Article

A single-cell transcriptomic atlas characterizes ageing tissues in the mouse

https://doi.org/10.1038/s41586-020-2496-1

Received: 5 June 2019

Accepted: 7 May 2020

Published online: 15 July 2020

Check for updates

The Tabula Muris Consortium*

Ageing is characterized by a progressive loss of physiological integrity, leading to impaired function and increased vulnerability to death[1]. Despite rapid advances over recent years, many of the molecular and cellular processes that underlie the progressive loss of healthy physiology are poorly understood[2]. To gain a better insight into these processes, here we generate a single-cell transcriptomic atlas across the lifespan of *Mus musculus* that includes data from 23 tissues and organs. We found cell-specific changes occurring across multiple cell types and organs, as well as age-related changes in the cellular composition of different organs. Using single-cell transcriptomic data, we assessed cell-type-specific manifestations of different hallmarks of ageing—such as senescence[3], genomic instability[4] and changes in the immune system[2]. This transcriptomic atlas—which we denote *Tabula Muris Senis*, or 'Mouse Ageing Cell Atlas'—provides molecular information about how the most important hallmarks of ageing are reflected in a broad range of tissues and cell types.

We performed single-cell RNA sequencing on more than 350,000 cells from male and female C57BL/6JN mice belonging to six age groups, ranging from 1 month (the equivalent of human early childhood) to 30 months (the equivalent of a human centenarian) (Fig. 1a). For all mice, we prepared single-cell suspensions of the bladder, bone marrow, brain (cerebellum, cortex, hippocampus and striatum), fat (brown, gonadal, mesenteric and subcutaneous), heart and aorta, kidney, large intestine, limb muscle and diaphragm, liver, lung, mammary gland, pancreas, skin, spleen, thymus, tongue and trachea. Data were collected for all six age groups using a microfluidic droplet method (droplet); the 3-month, 18-month and 24-month time points were also analysed using single cells sorted in microtitre well plates (fluorescence-activated cell sorting; FACS) (Extended Data Figs. 1–3, Supplementary Tables 1, 2). Owing to technical constraints, not every tissue was analysed at all time points; a complete list is provided in Extended Data Fig. 4a. The droplet data enable large numbers of cells to be analysed using 3′ end counting, whereas the FACS data allow for higher-sensitivity measurements over smaller numbers of cells as well as enabling the acquisition of sequence information across the entire transcript length. The analysis of multiple organs from the same mouse enables us to obtain data that is controlled for age, environment and epigenetic effects.

Data from the 3-month time point—which has previously been published and constitutes the *Tabula Muris*[5]—represents approximately 20% of the cells in the entire dataset, and was used as a basis from which to perform semi-automated cell-type annotation of the data from the additional time points (Fig. 1b, Extended Data Fig. 4b). Using this approach, we were able to automatically annotate more than 70% of the cells. All the automated cell annotations were reviewed and approved by human experts, and the remaining cells were annotated by hand, creating one of the largest manually curated single-cell transcriptomic resources in existence. Many of these cell types have not previously been obtained in pure populations, and these data provide a wealth of new information about their characteristic gene expression profiles. Out of 529,823 total cells sequenced, 110,824 cells for FACS and 245,389 cells for droplet passed our strict filtering criteria (Extended Data Fig. 4b) and were annotated (Extended Data Fig. 2a, b), which was carried out separately for each tissue and method. The remaining cells are also included in the online dataset but were not used for further analysis here. To investigate whether cell annotations were consistent across the entire organism, we used the bbknn batch-alignment algorithm[6] to correct for method-associated batch effects (Supplementary Table 3). After batch correction, we clustered all cells using an unbiased, graph-based clustering approach[7,8] (Fig. 1c, d) and assessed the co-occurrence of similarly annotated cells in the same clusters. For example, cells annotated as B cells or endothelial cells tend to occupy the same clusters irrespective of their tissue of origin or the method with which they were processed (Fig. 1e, f, Extended Data Fig. 1g–l).

The *Tabula Muris Senis* enables the discovery of ageing-related changes in specific cell types. Single-cell data enables us to resolve whether gene expression changes observed in bulk experiments are due to changes in gene expression in each cell of the population, or whether the gene expression in each cell stays constant but the number of cells of that type changes, or both. In a global analysis of gene expression changes using the *Tabula Muris Senis* and bulk RNA sequencing from tissues[9], we observed that—in many cases—changes in gene expression are due to both changes in the numbers of cells in a population and changes in the gene expression levels in each cell (Extended Data Fig. 5a, b). As one specific example, we investigated how the fraction of cells that express *Cdkn2a* changes with age. The expression of *Cdkn2a* and its protein product p16 is one of the most frequently used markers of senescence[10] and is an important hallmark of ageing[11]. The proportion of cells expressing *Cdkn2a* more than doubled in older mice compared with younger mice according to analysis by both FACS (Fig. 2a) and droplet (Fig. 2b) methods; this was accompanied by a twofold increase

*A list of members and their affiliations appears at the end of the paper.

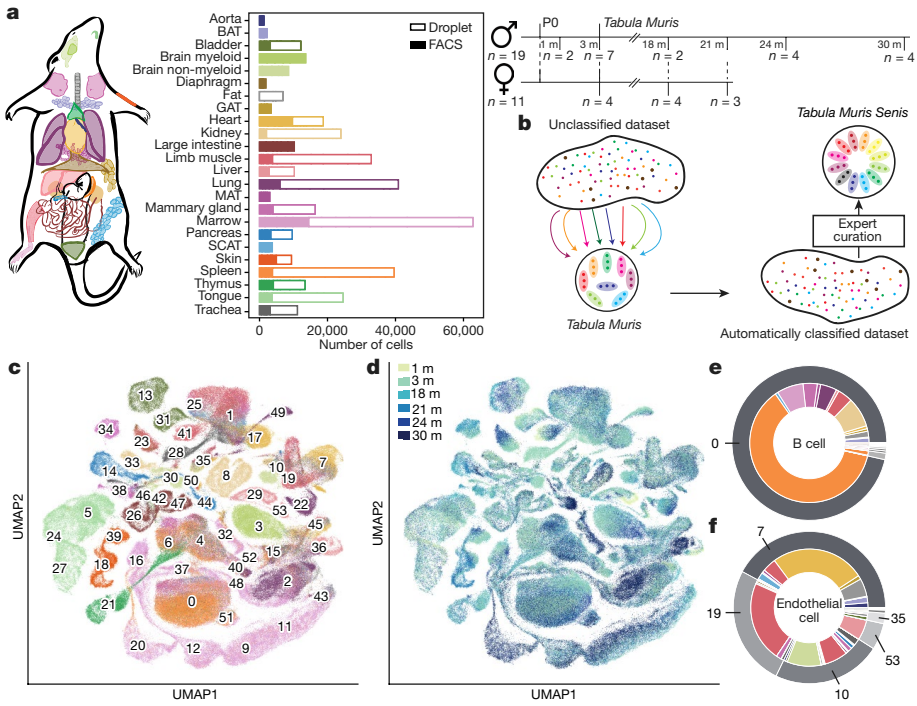

Fig. 1 | Overview of the *Tabula Muris Senis*. **a**, A total of 23 organs from 19 male and 11 female mice were analysed at 6 different time points. The bar plot shows the number of sequenced cells per organ prepared by FACS ($n = 23$ organs) and by microfluidic droplets ($n = 16$ organs). For the droplet dataset the fat sub-tissues were processed together (Fat = BAT + GAT + MAT + SCAT; BAT, brown adipose tissue; GAT, gonadal adipose tissue; MAT, mesenteric adipose tissue; SCAT, subcutaneous adipose tissue). **b**, Annotation workflow. Data were clustered together across all time points. We used the *Tabula Muris* (3-month time point) as a reference for the automated pipeline and the annotations were manually curated by tissue experts. **c**, **d**, Uniform manifold approximation and projection (UMAP) plot of all cells, coloured by organ and overlaid with the Louvain cluster numbers (**c**) and age (**d**); $n = 356{,}213$ individual cells. See Extended Data Fig. 4c, d for the colour dictionaries. **e**, **f**, B cells (**e**) and endothelial cells (**f**) independently annotated for each organ cluster together by unbiased whole-transcriptome Louvain clustering, irrespective of the organ in which they were found.

in the expression levels of p16 in cells in which it was expressed (Fig. 2c, d). Notably, in 30-month-old mice the fraction of cells that expressed p16 was smaller than in 24-month-old mice, perhaps because long-living animals have a slower rate of senescence. Using a list of previously characterized senescence markers[12–15], we plotted the fraction of cells expressing each marker across all age groups (Supplementary Table 4). *Cdkn2a* has the highest correlation between ageing and the fraction of cells in which it is expressed; other genes with positive correlation include *E2f2*[16], *Lmnb1*[17,18], *Tnf* and *Itgax*[19]. For some genes, including members of the Sirt family (*Sirt3*, *Sirt4* and *Sirt5*), the fraction of cells in which they were expressed was found to decrease with age; this is consistent with previous literature finding that sirtuins—the protein products of Sirt genes—are essential in delaying cellular senescence[20,21].

The cellular composition of each tissue type tends to vary with age. We investigated changes in the cellular composition of tissues for which data from at least three time points was available (Supplementary Table 5). Because dissociation does not affect all cell types in a tissue equally, changes in the relative composition of a given cell type with age are more meaningful than comparing proportions of different cell types at a single age[22–24]. The bladder shows pronounced changes in cell-type composition with age (Fig. 2e): whereas the mesenchymal compartment of this tissue decreases by a factor of three over the lifetime of the mouse (Fig. 2e, left), the urothelial compartment increases by a similar amount (Fig. 2e, right). The observation that the proportion of bladder urothelial cells increases with age is concordant with known age-related urothelial changes[25]. Using differential gene expression analysis to assess overall changes in tissues with age, we found that stromal-associated genes (*Col1a1*, *Col1a2*, *Col3a1* and *Dcn*) are downregulated while epithelial-associated genes (*Krt15*, *Krt18* and *Sfn*) are upregulated, supporting the compositional observations (Fig. 2f, Supplementary Table 6). The decline of the endothelial population suggests that bladder ageing in mice might be associated with lower organ vascularization, which is consistent with recent findings[26,27] and with the observed downregulation of vasculature-associated genes *Htra1* and *Fos* (Fig. 2f, Supplementary Table 6). The increase in the leukocyte population could indicate an inflammatory tissue microenvironment, a common hallmark of ageing that is consistent with literature on overactive bladders[28] and is supported by a significant overexpression of *Lgals3*, *Igfbp2* and *Ly6d* across the tissue (Fig. 2f, Supplementary Table 6), as well as by the overexpression of genes associated with immune response—such as *Tnfrsf12a* and *Cdkn1a*—in both bladder (mesenchymal) cells and bladder urothelial cells (Supplementary Table 6). Moreover, when comparing across ages, we observed that old leukocytes show increased expression of pro-inflammatory markers—such as *Cd14*, *Lgals3* and *Tnfrsf12a*—and decreased expression of anti-inflammatory markers such as *Cd9* and *Cd81* (Supplementary Table 6).

Age-related changes in the kidney include a decrease in the relative abundance of mesangial cells, capillary endothelial cells, loop of Henle ascending limb epithelial cells and loop of Henle thick ascending limb epithelial cells (Fig. 2g). Both mesangial cells and capillary endothelial cells are core glomerular cells, and the reduction in their relative abundances with age (Fig. 2g, top)—together with a tissue-wide reduction of *Egf* and *Atp1a1* expression (Fig. 2h, Supplementary Table 6)—suggest an impaired glomerular filtration rate[29,30]. Notably, local *Atp1a1* expression increases with age in both capillary endothelial cells and mesangial cells, suggesting that a compensation mechanism counteracts the effects of the declining proportion of these cells with age. This finding is reinforced

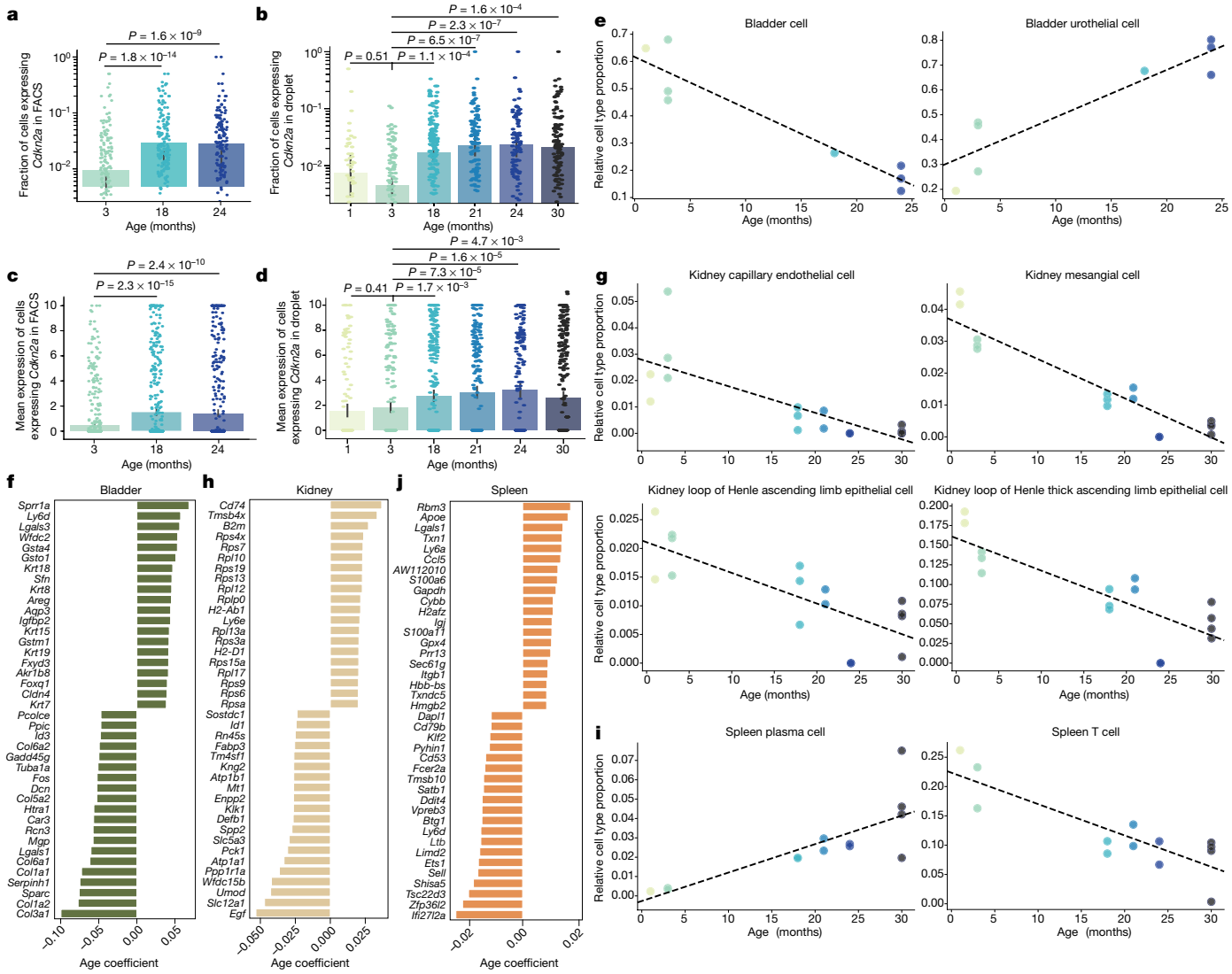

Fig. 2 | Cellular changes during ageing. a, **b**, Bar plot showing the fractions of cells expressing *Cdkn2a* in each age group for FACS (**a**) and droplet (**b**) experiments. **c**, **d**, Bar plot of the median expression of *Cdkn2a* for the cells that do express the gene at each age group for FACS (**c**) and droplet (**d**) experiments. The *y* axis shows log-transformed and scaled values. All data are expressed as mean ± s.d. with individual data points shown. *P* values were obtained using a Mann–Whitney–Wilcoxon rank-sum two-sided test. $n = 44{,}518$, 34,027 and 31,551 individual cells for FACS at 3, 18 and 24 months, respectively; $n = 25{,}980$, 45,602, 44,645, 35,828, 37,660 and 55,674 individual cells for droplet at 1, 3, 18, 21, 24 and 30 months, respectively. **e**, **g**, **i**, The relative abundances of bladder cells (**e**, left) and bladder urothelial cells (**e**, right), kidney capillary endothelial cells (**g**, top left), mesangial cells (**g**, top right), loop of Henle ascending limb epithelial cells (**g**, bottom left) and loop of Henle thick ascending limb epithelial cells (**g**, bottom right), and spleen plasma cells (**i**, left) and T cells (**i**, right) change significantly with age. $P < 0.05$ and $r^2 > 0.7$ for a hypothesis test with the null hypothesis that the slope is zero, using two-sided Wald test with *t*-distribution of the test statistic. **f**, **h**, **j**, Top 20 upregulated and top 20 downregulated genes in bladder (**f**), kidney (**h**) and spleen (**j**) computed using MAST[51], treating age as a continuous covariate while controlling for sex and technology. Genes were classified as significant under a false-discovery rate (FDR) threshold of 0.01 and an age coefficient threshold of 0.005 (corresponding to an approximately 10%-fold change). For **f**, $n = 970$, 3,804, 2,739 and 3,864 individual cells for bladder at 1, 3, 18 and 24 months, respectively; for **h**, $n = 2{,}488$, 2,832, 3,806, 2,257, 6,384 and 5,713 individual cells for kidney at 1, 3, 18, 21, 24 and 30 months, respectively; for **j**, $n = 2{,}986$, 8,839, 7,141, 6,395, 5,245 and 8,946 individual cells for spleen at 1, 3, 18, 21, 24 and 30 months, respectively. The *P* values for the cell type compositional changes are shown in Supplementary Table 5.

by the results of differential gene expression analysis, suggesting that the expression of *Umod*—which encodes uromodulin, the most abundant protein in urine[31]—is also reduced across the tissue. The protein uromodulin is produced by the epithelial cells that line the thick ascending limb, and therefore—given the relative decrease in the proportion of epithelial cells in the ascending and the thick ascending limb—our results suggest that normal kidney functions are impaired[32] (Fig. 2g, bottom, Fig. 2h, Supplementary Table 6). As with *Atp1a1*, we see that the expression of *Umod* increases in a cell type that becomes less abundant with age, leading to an overall reduction of its expression in the organ.

In the spleen, the proportion of T cells decreases with age while the relative amount of plasma cells increases (Fig. 2i). This is supported by the upregulation of B cell and plasma cell marker genes (*Cd79a* and *Jchain* (also known as *Igj*), respectively; Fig. 2j, Supplementary Table 6) and the downregulation of *Cd3d* (Fig. 2j, Supplementary Table 6). Similarly, in the mammary gland we observed a decline of the T cell population (Extended Data Fig. 5c). Age-related decline of T cell populations has been associated with increased risk of infectious disease and cancer[33], and our results suggest that such a decline might also occur in the spleen and the mammary gland. Moreover, genes encoding AP1

transcription factors[34] (*Junb*, *Jund* and *Fos*) were upregulated with age (Extended Data Fig. 5d, Supplementary Table 6), consistent with the observation that normal involution of the mammary gland is accompanied by increased expression of this gene family[35].

The tissue composition of the liver also changes with age. We observed an age-related decrease in the relative number of hepatocytes (Extended Data Fig. 6a–d), which is supported by the reduction in the expression of albumin (*Alb*; Extended Data Fig. 6e, Supplementary Table 6). Differential gene expression analysis revealed an increased immune signature, as illustrated by the overexpression of *H2-Aa*, *H2-Ab1*, *H2-D1*, *H2-Eb1*, *Cd74*, *Lyz2* and others (Extended Data Fig. 6e). Previous findings suggested that pro-inflammatory macrophages drive cellular senescence, and identified the gene *Il1b* as showing markedly different expression in the liver with age[12] (Extended Data Fig. 6f). We performed in situ RNA staining in liver Kupffer cells (Extended Data Fig. 6g) with *Clec4f* and found that the number of *Clec4f*-positive cells does not change with age, consistent with the results of the tissue composition analysis (Extended Data Fig. 6h, Supplementary Table 7). However, when co-staining with *Il1b*, we found that the number of cells expressing both *Clec4f* and *Il1b* increased with age (Extended Data Fig. 6h–j). The expression of *Il1b* is low under normal physiological conditions[36]. Specific blocking of IL1-RI in hepatocytes has been shown to attenuate cell death after injury, supporting the idea that increased expression of *Il1b* in Kupffer cells is typically a poor prognostic[37]. Liver sinusoidal endothelial cells (LSECs) have a unique role in immune defence, being the main carriers of the mannose receptor (MRC1) in this organ[38] (Extended Data Fig. 6k). We identified increased expression of *Mrc1* with age in Kupffer cells, whereas the overall expression of *Mrc1* in liver endothelial cells decreased with age (Supplementary Table 6). By performing in situ RNA staining for *Mrc1* alongside the classical LSEC marker *Pecam1* (Extended Data Fig. 6l, Supplementary Table 7), we found that the number of *Mrc1*-expressing LSECs increased with age (Extended Data Fig. 6m–o). Although *Mrc1* expression did not increase with age in LSECs (Supplementary Table 6), the overall number of cells expressing *Mrc1* did increase significantly with age (Extended Data Fig. 6n). LSECs have been found to have a reduced endocytic capacity in aged livers, and it has been suggested that LSECs proliferate after injury or that bone-marrow-derived LSEC progenitors are recruited to the liver. This suggests that changes in the gene signatures of LSECs with age are closely linked with the function of these cells in immune response.

Genomic instability is among the most widely studied hallmarks of ageing[1], and full-length transcript data enables analysis of the accumulation of somatic mutations with age. We used the Genome Analysis ToolKit[39] to identify single-nucleotide polymorphisms across all FACS samples simultaneously[40,41] (Supplementary Table 8). We focused on genes that were expressed in at least 75% of cells for each age group within a particular tissue, and observed an age-related increase in the number of mutations across all of the organs we analysed (Fig. 3, Extended Data Fig. 7a, c, e)—tongue and bladder were the most affected. We controlled for sequencing coverage and gene expression levels (Extended Data Fig. 8a, c, e), and verified that the number of mutations exceeded those expected from amplification and sequencing errors, which can be estimated using External RNA Controls Consortium (ERCC) controls that were spiked into each well[42] (Fig. 3, Extended Data Figs. 7b, d, f, 8b, d, f). Despite the fact that it is difficult to infer absolute genome-wide mutation rates from the transcriptome, which is known to overstate apparent mutational rates for various reasons[42], the observed trend is a useful indirect estimate of mutational frequency and genome stability.

Ageing also affects the immune system[2], so we analysed clonal relationships between B cells and T cells throughout the organism. We computationally reconstructed the sequence of the B cell receptor and the T cell receptor for B cells and T cells present in the FACS data using singlecell-ige and TraCeR, respectively[43,44]. B cell receptors were assembled for 6,050 cells (Fig. 4a, Extended Data Fig. 9a) and T cell receptors for 6,000 cells (Fig. 4b, Extended Data Fig. 9b). The number of cells with assembled B cell receptors was 1,818 for 3-month-old, 1,356 for 18-month-old and 2,876 for 24-month-old mice. We parsed the singlecell-ige[43] output to define B cell clonotypes on the basis of the sequence of the assembled B cell receptor (Supplementary Table 9) and found that, whereas most of the cells at 3 months were not part of a clone (9% were part of a clonal family), the number of B cells belonging to a clonotype doubled at 18 months (20%) when compared to 3 months, and doubled again from 18 months to 24 months (around 38%). The number of cells with assembled T cell receptors was roughly equal between 3-month-old, 18-month-old and 24-month-old mice (2,076, 2,056 and 1,868 cells, respectively). Clonotype assignment is part of the output obtained by TraCeR[44] (Supplementary Table 9). Notably, only around 3% (55 out of 1,895) of the cells at 3 months were part of a clone. At 18 months and 24 months, this value increased to around 23% (479 out of 2,056) and around 20% (348 out of 1,780) of the cells, respectively, again indicating an increase in clonality of the T cell repertoire at later ages. These changes in clonality for both B cell and T cell repertoires are noteworthy, because they suggest that the immune system of a 24-month-old mouse is less likely to respond to new pathogens. This corroborates literature reports suggesting that older individuals have a higher vulnerability to new infections and lower benefits from vaccination compared with younger individuals[45,46].

Finally, we computed an overall diversity score to identify which cell types were more susceptible to changes with age (Extended Data Fig. 10). The diversity score is computed as the Shannon entropy of the cluster assignment and then regressed against age to provide a *P* value (see Methods). We observed significant changes in diversity for cells of the immune system that originate from the brain and the kidney (Fig. 4c, Extended Data Fig. 11a, b). These results were not confounded by the number of genes expressed per cell (Extended Data Fig. 11c, d). In brain myeloid microglial cells, the majority of young (3 month) microglia occupy clusters 1 and 6, whereas old (18 month and 24 month) microglia constitute the vast majority of cells in clusters 10,

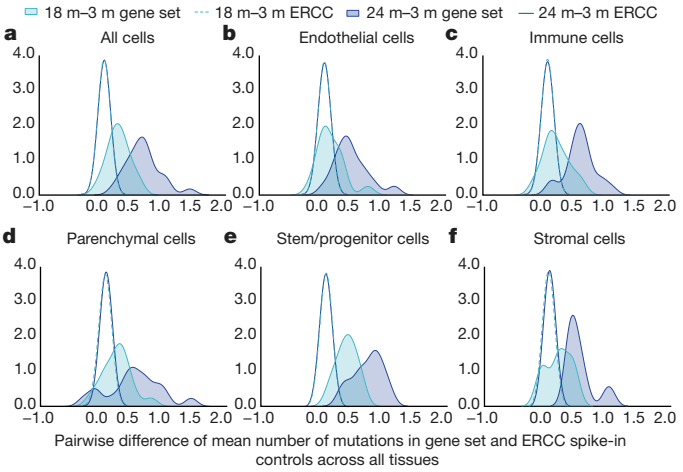

Fig. 3 | Mutational burden across tissues in ageing mice. a–f, Distribution of the difference of the mean mutation in the gene set (and ERCC spike-in controls) per cell between 24 months and 3 months and between 18 months and 3 months for all tissues and cells (**a**) and with the cell types split into five functional groups: endothelial cells (**b**), immune cells (**c**), parenchymal cells (**d**), stem/progenitor cells (**e**) and stromal cells (**f**). Filled and solid line distributions correspond to the mean mutation difference in gene set. White and dashed line distributions correspond to the mean mutation difference in ERCC spike-in controls. Note that the mean mutation difference in ERCC spike-in controls overlaps for both age groups. The *y* axis corresponds to the kernel density estimation (arbitrary units).

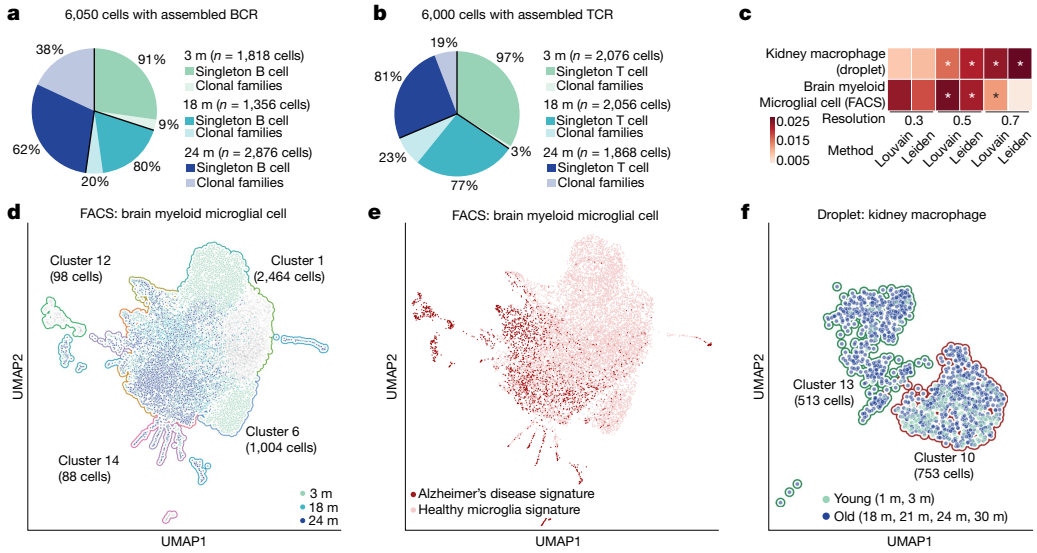

Fig. 4 | The ageing immune system. a, **b**, B cell (**a**) and T cell (**b**) clonal families. The pie charts show the proportion of singleton B cells and B cells and that are part of clonal families (**a**) and singleton T cells and T cells that are part of clonal families (**b**) at 3 months, 18 months and 24 months. See Extended Data Fig. 9 for clonal networks. BCR, B cell receptor; TCR, T cell receptor. **c**, Diversity scores for the two cell types for which this score changes significantly with age. **d**, UMAP plot of the brain myeloid microglial cell Leiden clusters (numbers) coloured by age. The relative cell composition of faded clusters does not change with age; that of the coloured clusters does change with age. **e**, UMAP plot of the brain myeloid microglial cells when scored using the microglia Alzheimer's disease signature (Supplementary Table 10). $n = 4,532$, 4,461 and 4,424 individual microglia cells for brain myeloid at 3 months, 18 months and 24 months, respectively. **f**, UMAP plot of the kidney macrophage Leiden clusters (numbers) coloured by age group. $n = 62$, 139, 264, 105, 284 and 553 individual macrophage cells for kidney at 1, 3, 18, 21, 24 and 30 months, respectively.

12 and 14 (Fig. 4d). Trajectory analysis suggests that young microglia go through an intermediate state, represented by the clusters mostly occupied by 18-month microglial cells, before acquiring the signature of old microglia (Extended Data Fig. 11e). Clusters 10, 12 and 14 mainly comprise 18-month and 24-month microglia. These cells upregulate major histocompatibility complex (MHC) class I genes (*H2-D1*, *H2-K1* and *B2m*), along with genes associated with degenerative disease (for example, *Fth1*)[47,48]. When compared with clusters 1 and 6—which contain mostly 3-month microglia—gene expression in clusters 10, 12 and 14 is enriched with interferon responsive or regulatory genes (for example, *Oasl2*, *Oas1a*, *Ifit3*, *Rtp4*, *Bst2*, *Stat1*, *Irf7*, *Ifitm3*, *Usp18*, *Ifi204* and *Ifit2*), suggesting an expansion of this small pro-inflammatory subset of microglia in the ageing brain[49]. Moreover, the list of differentially expressed genes between 'young' and 'old' clusters resembles the previously reported Alzheimer's disease-specific microglial signature[47], with 55 out of the top 200 differential expressed genes shared between the two differential gene expression lists (Fig. 4e, Supplementary Table 10). Regarding kidney macrophages, we found two clusters for which the composition changed markedly with age. Cluster 10 is primarily composed of cells from 1-month-old and 3-month-old mice, whereas cluster 13 is mostly composed of cells from18-month-old, 21-month-old, 24-month-old and 30-month old mice (Fig. 4f). Differential gene expression revealed that cluster 10 is enriched for an M2-macrophage gene signature (for example, *Il10*, *H2-Eb1*, *H2-Ab1*, *H2-Aa*, *Cd74*, *C1qa*, *Cxcl16*, *Hexb*, *Cd81*, *C1qb* and *Cd72*) whereas cluster 13 resembles a M1-proinflammatory macrophage state[50] (for example, *Hp*, *Itgal*, *Msrb1* and *Gngt2*) (Extended Data Fig. 11f, Supplementary Table 10).

The *Tabula Muris Senis* is a comprehensive resource for the cell biology community that offers a detailed molecular and cell-type-specific portrait of ageing. We view such a cell atlas as an essential companion to the genome: the genome provides a blueprint for the organism, but does not explain how genes are used in a cell-type-specific manner or how the usage of genes changes over the lifetime of the organism. The cell atlas provides a deep characterization of phenotype and physiology and serves as a reference for understanding many aspects of the changes in cell biology that occur in mammals during their lifespan.

Online content

Any methods, additional references, Nature Research reporting summaries, source data, extended data, supplementary information, acknowledgements, peer review information; details of author contributions and competing interests; and statements of data and code availability are available at https://doi.org/10.1038/s41586-020-2496-1.

1. López-Otín, C., Blasco, M. A., Partridge, L., Serrano, M. & Kroemer, G. The hallmarks of aging. *Cell* **153**, 1194–1217 (2013).
2. Nikolich-Žugich, J. The twilight of immunity: emerging concepts in aging of the immune system. *Nat. Immunol.* **19**, 10–19 (2018).
3. Campisi, J. Aging, cellular senescence, and cancer. *Annu. Rev. Physiol.* **75**, 685–705 (2013).
4. Vijg, J. & Suh, Y. Genome instability and aging. *Annu. Rev. Physiol.* **75**, 645–668 (2013).
5. The Tabula Muris Consortium. Single-cell transcriptomics of 20 mouse organs creates a *Tabula Muris*. *Nature* **562**, 367–372 (2018).
6. Polański, K. et al. BBKNN: fast batch alignment of single cell transcriptomes. *Bioinformatics* **36**, 964–965 (2020).
7. Blondel, V. D., Guillaume, J.-L., Lambiotte, R. & Lefebvre, E. Fast unfolding of communities in large networks. *J. Stat. Mech.* P10008 (2008).
8. Traag, V. A., Waltman, L. & van Eck, N. J. From Louvain to Leiden: guaranteeing well-connected communities. *Sci. Rep.* **9**, 5233 (2019).
9. Schaum, N. et al. The murine transcriptome reveals global aging nodes with organ-specific phase and amplitude. Preprint at https://www.biorxiv.org/content/10.1101/662254v1 (2019).
10. Rayess, H., Wang, M. B. & Srivatsan, E. S. Cellular senescence and tumor suppressor gene p16. *Int. J. Cancer* **130**, 1715–1725 (2012).
11. Hernandez-Segura, A., Nehme, J. & Demaria, M. Hallmarks of cellular senescence. *Trends Cell Biol.* **28**, 436–453 (2018).
12. Covarrubias, A. J. et al. Aging-related inflammation driven by cellular senescence enhances NAD consumption via activation of CD38+ pro-inflammatory macrophages. Preprint at https://www.biorxiv.org/content/10.1101/609438v2 (2019).
13. Nagano, T. et al. Identification of cellular senescence-specific genes by comparative transcriptomics. *Sci. Rep.* **6**, 31758 (2016).
14. Carnero, A. in *Cell Senescence*. Methods in Molecular Biology (Methods and Protocols) Vol. 965 (eds Galluzzi, L., Vitale, I., Kepp, O. & Kroemer, G.) (Humana, 2013).
15. Wang, A. S. & Dreesen, O. Biomarkers of cellular senescence and skin aging. *Front. Genet.* **9**, 247 (2018).
16. Vernier, M. et al. Regulation of E2Fs and senescence by PML nuclear bodies. *Genes Dev.* **25**, 41–50 (2011).

17. Dreesen, O. et al. Lamin B1 fluctuations have differential effects on cellular proliferation and senescence. *J. Cell Biol.* **200**, 605–617 (2013).
18. Shah, P. P. et al. Lamin B1 depletion in senescent cells triggers large-scale changes in gene expression and the chromatin landscape. *Genes Dev.* **27**, 1787–1799 (2013).
19. Li, P. et al. The inflammatory cytokine TNF-α promotes the premature senescence of rat nucleus pulposus cells via the PI3K/Akt signaling pathway. *Sci. Rep.* **7**, 42938 (2017).
20. Saunders, L. R. & Verdin, E. Sirtuins: critical regulators at the crossroads between cancer and aging. *Oncogene* **26**, 5489–5504 (2007).
21. Lee, S.-H., Lee, J.-H., Lee, H.-Y. & Min, K.-J. Sirtuin signaling in cellular senescence and aging. *BMB Rep.* **52**, 24–34 (2019).
22. van den Brink, S. C. et al. Single-cell sequencing reveals dissociation-induced gene expression in tissue subpopulations. *Nat. Methods* **14**, 935–936 (2017).
23. Tung, P.-Y. et al. Batch effects and the effective design of single-cell gene expression studies. *Sci. Rep.* **7**, 39921 (2017).
24. Nguyen, Q. H., Pervolarakis, N., Nee, K. & Kessenbrock, K. Experimental considerations for single-cell RNA sequencing approaches. *Front. Cell Dev. Biol.* **6**, 108 (2018).
25. Daly, D. M. et al. Age-related changes in afferent pathways and urothelial function in the male mouse bladder. *J. Physiol. (Lond.)* **592**, 537–549 (2014).
26. Burmeister, D. M., AbouShwareb, T., Bergman, C. R., Andersson, K.-E. & Christ, G. J. Age-related alterations in regeneration of the urinary bladder after subtotal cystectomy. *Am. J. Pathol.* **183**, 1585–1595 (2013).
27. Andersson, K.-E., Boedtkjer, D. B. & Forman, A. The link between vascular dysfunction, bladder ischemia, and aging bladder dysfunction. *Ther. Adv. Urol.* **9**, 11–27 (2017).
28. Suskind, A. M. The aging overactive bladder: a review of aging-related changes from the brain to the bladder. *Curr. Bladder Dysfunct. Rep.* **12**, 42–47 (2017).
29. Zhang, D. et al. Downregulation of ATP1A1 promotes cancer development in renal cell carcinoma. *Clin. Proteomics* **14**, 15 (2017).
30. Isaka, Y. Epidermal growth factor as a prognostic biomarker in chronic kidney diseases. *Ann. Transl. Med.* **4**, S62 (2016).
31. Devuyst, O., Olinger, E. & Rampoldi, L. Uromodulin: from physiology to rare and complex kidney disorders. *Nat. Rev. Nephrol.* **13**, 525–544 (2017).
32. Tokonami, N. et al. Uromodulin is expressed in the distal convoluted tubule, where it is critical for regulation of the sodium chloride cotransporter NCC. *Kidney Int.* **94**, 701–715 (2018).
33. Palmer, S., Albergante, L., Blackburn, C. C. & Newman, T. J. Thymic involution and rising disease incidence with age. *Proc. Natl Acad. Sci. USA* **115**, 1883–1888 (2018).
34. Shen, Q. et al. The AP-1 transcription factor regulates postnatal mammary gland development. *Dev. Biol.* **295**, 589–603 (2006).
35. Girnius, N., Edwards, Y. J. K. & Davis, R. J. The cJUN NH_2-terminal kinase (JNK) pathway contributes to mouse mammary gland remodeling during involution. *Cell Death Differ.* **25**, 1702–1715 (2018).
36. Tan, Q. et al. The role of IL-1 family members and Kupffer cells in liver regeneration. *BioMed Res. Int.* **2016**, 6495793 (2016).
37. Gehrke, N. et al. Hepatocyte-specific deletion of IL1-RI attenuates liver injury by blocking IL-1 driven autoinflammation. *J. Hepatol.* **68**, 986–995 (2018).
38. Liu, Y., Gardner, C. R., Laskin, J. D. & Laskin, D. L. Classical and alternative activation of rat hepatic sinusoidal endothelial cells by inflammatory stimuli. *Exp. Mol. Pathol.* **94**, 160–167 (2013).
39. McKenna, A. et al. The Genome Analysis Toolkit: a MapReduce framework for analyzing next-generation DNA sequencing data. *Genome Res.* **20**, 1297–1303 (2010).
40. DePristo, M. A. et al. A framework for variation discovery and genotyping using next-generation DNA sequencing data. *Nat. Genet.* **43**, 491–498 (2011).
41. Auwera, G. A. et al. From FastQ data to high-confidence variant calls: the Genome Analysis Toolkit best practices pipeline. *Curr. Protoc. Bioinformatics* **43**, 11.10.1–11.10.33 (2013).
42. Zook, J. M., Samarov, D., McDaniel, J., Sen, S. K. & Salit, M. Synthetic spike-in standards improve run-specific systematic error analysis for DNA and RNA sequencing. *PLoS ONE* **7**, e41356 (2012).
43. Croote, D., Darmanis, S., Nadeau, K. C. & Quake, S. R. High-affinity allergen-specific human antibodies cloned from single IgE B cell transcriptomes. *Science* **362**, 1306–1309 (2018).
44. Stubbington, M. J. T. et al. T cell fate and clonality inference from single-cell transcriptomes. *Nat. Methods* **13**, 329–332 (2016).
45. Goronzy, J. J. & Weyand, C. M. Understanding immunosenescence to improve responses to vaccines. *Nat. Immunol.* **14**, 428–436 (2013).
46. Goronzy, J. J. & Weyand, C. M. Successful and maladaptive T cell aging. *Immunity* **46**, 364–378 (2017).
47. Keren-Shaul, H. et al. A unique microglia type associated with restricting development of Alzheimer's disease. *Cell* **169**, 1276–1290.e17 (2017).
48. Li, Q. et al. Developmental heterogeneity of microglia and brain myeloid cells revealed by deep single-cell RNA sequencing. *Neuron* **101**, 207–223.e10 (2019).
49. Hammond, T. R. et al. Single-cell RNA sequencing of microglia throughout the mouse lifespan and in the injured brain reveals complex cell-state changes. *Immunity* **50**, 253–271.e6 (2019).
50. Jablonski, K. A. et al. Novel markers to delineate murine M1 and M2 macrophages. *PLoS ONE* **10**, e0145342 (2015).
51. Finak, G. et al. MAST: a flexible statistical framework for assessing transcriptional changes and characterizing heterogeneity in single-cell RNA sequencing data. *Genome Biol.* **16**, 278 (2015).

The Tabula Muris Consortium

Nicole Almanzar[1], Jane Antony[2], Ankit S. Baghel[2], Isaac Bakerman[2,3,4], Ishita Bansal[2], Ben A. Barres[5], Philip A. Beachy[2,6,7,8], Daniela Berdnik[9], Biter Bilen[10], Douglas Brownfield[6], Corey Cain[11], Charles K. F. Chan[12], Michelle B. Chen[13], Michael F. Clarke[2], Stephanie D. Conley[14], Spyros Darmanis[14]✉, Aaron Demers[14], Kubilay Demir[2,7], Antoine de Morree[10], Tessa Divita[14], Haley du Bois[9], Hamid Ebadi[14], F. Hernán Espinoza[6], Matt Fish[2,7,8], Qiang Gan[10], Benson M. George[2], Astrid Gillich[6], Rafael Gòmez-Sjöberg[14], Foad Green[14], Geraldine Genetiano[14], Xueying Gu[8], Gunsagar S. Gulati[2], Oliver Hahn[10], Michael Seamus Haney[10], Yan Hang[8], Lincoln Harris[14], Mu He[15], Shayan Hosseinzadeh[14], Albin Huang[10], Kerwyn Casey Huang[13,14,16], Tal Iram[10], Taichi Isobe[2], Feather Ives[14], Robert C. Jones[13], Kevin S. Kao[2], Jim Karkanias[14], Guruswamy Karnam[17], Andreas Keller[10,18], Aaron M. Kershner[2], Nathalie Khoury[10], Seung K. Kim[8,19], Bernhard M. Kiss[2,20], William Kong[2], Mark A. Krasnow[6,7], Maya E. Kumar[21,22], Christin S. Kuo[1], Jonathan Lam[8], Davis P. Lee[9], Song E. Lee[10], Benoit Lehallier[10], Olivia Leventhal[9], Guang Li[4,23], Qingyun Li[5], Ling Liu[10], Annie Lo[14], Wan-Jin Lu[2,6], Maria F. Lugo-Fagundo[9], Anoop Manjunath[2], Andrew P. May[14], Ashley Maynard[14], Aaron McGeever[14], Marina McKay[14], M. Windy McNerney[24,25], Bryan Merrill[16], Ross J. Metzger[26,27], Marco Mignardi[13], Dullei Min[1], Ahmad N. Nabhan[6], Norma F. Neff[14], Katharine M. Ng[6], Patricia K. Nguyen[2,3,4], Joseph Noh[2], Roel Nusse[6,7,8], Róbert Pálovics[10], Rasika Patkar[17], Weng Chuan Peng[8,38], Lolita Penland[14], Angela Oliveira Pisco[14], Katherine Pollard[28], Robert Puccinelli[14], Zhen Qi[2], Stephen R. Quake[13,14]✉, Thomas A. Rando[9,10,29], Eric J. Rulifson[8], Nicholas Schaum[2,10], Joe M. Segal[17], Shaheen S. Sikandar[2], Rahul Sinha[2,30,31,32], Rene V. Sit[14], Justin Sonnenburg[14,16], Daniel Staehli[10], Krzysztof Szade[2,33], Michelle Tan[14], Weilun Tan[14], Cristina Tato[14], Krissie Tellez[8], Laughing Bear Torrez Dulgeroff[2], Kyle J. Travaglini[6], Carolina Tropini[16,39,40,41], Margaret Tsui[17], Lucas Waldburger[14], Bruce M. Wang[17], Linda J. van Weele[2], Kenneth Weinberg[1], Irving L. Weissman[2,30,31,32], Michael N. Wosczyna[10], Sean M. Wu[2,3,23], Tony Wyss-Coray[9,10,29,34]✉, Jinyi Xiang[1], Soso Xue[13], Kevin A. Yamauchi[14], Andrew C. Yang[13], Lakshmi P. Yerra[10], Justin Youngyunpipatkul[14], Brian Yu[14], Fabio Zanini[13], Macy E. Zardeneta[9], Alexander Zee[14], Chunyu Zhao[14], Fan Zhang[26,27], Hui Zhang[9], Martin Jinye Zhang[35,36], Lu Zhou[5] & James Zou[14,35,37]

[1]Department of Pediatrics, Pulmonary Medicine, Stanford University School of Medicine, Stanford, CA, USA. [2]Institute for Stem Cell Biology and Regenerative Medicine, Stanford University School of Medicine, Stanford, CA, USA. [3]Stanford Cardiovascular Institute, Stanford University School of Medicine, Stanford, CA, USA. [4]Division of Cardiovascular Medicine, Department of Medicine, Stanford University School of Medicine, Stanford, CA, USA. [5]Department of Neurobiology, Stanford University School of Medicine, Stanford, CA, USA. [6]Department of Biochemistry, Stanford University School of Medicine, Stanford, CA, USA. [7]Howard Hughes Medical Institute, Chevy Chase, MD, USA. [8]Department of Developmental Biology, Stanford University School of Medicine, Stanford, CA, USA. [9]Veterans Administration Palo Alto Healthcare System, Palo Alto, CA, USA. [10]Department of Neurology and Neurological Sciences, Stanford University School of Medicine, Stanford, CA, USA. [11]Flow Cytometry Core, Veterans Administration Palo Alto Healthcare System, Palo Alto, CA, USA. [12]Department of Surgery, Division of Plastic and Reconstructive Surgery, Stanford University, Stanford, CA, USA. [13]Department of Bioengineering, Stanford University, Stanford, CA, USA. [14]Chan Zuckerberg Biohub, San Francisco, CA, USA. [15]Department of Physiology, University of California, San Francisco, CA, USA. [16]Department of Microbiology & Immunology, Stanford University School of Medicine, Stanford, CA, USA. [17]Department of Medicine and Liver Center, University of California San Francisco, San Francisco, CA, USA. [18]Clinical Bioinformatics, Saarland University, Saarbrücken, Germany. [19]Department of Medicine and Stanford Diabetes Research Center, Stanford University, Stanford, CA, USA. [20]Department of Urology, Stanford University School of Medicine, Stanford, CA, USA. [21]Sean N. Parker Center for Asthma and Allergy Research, Stanford University School of Medicine, Stanford, CA, USA. [22]Department of Medicine, Division of Pulmonary and Critical Care, Stanford University School of Medicine, Stanford, CA, USA. [23]Department of Developmental Biology, University of Pittsburgh School of Medicine, Pittsburgh, PA, USA. [24]Mental Illness Research Education and Clinical Center, Veterans Administration Palo Alto Healthcare System, Palo Alto, CA, USA. [25]Department of Psychiatry, Stanford University School of Medicine, Stanford, CA, USA. [26]Vera Moulton Wall Center for Pulmonary and Vascular Disease, Stanford University School of Medicine, Stanford, CA, USA. [27]Department of Pediatrics, Division of Cardiology, Stanford University School of Medicine, Stanford, CA, USA. [28]Department of Epidemiology and Biostatistics, University of California, San Francisco, CA, USA. [29]Paul F. Glenn Center for the Biology of Aging, Stanford University School of Medicine, Stanford, CA, USA. [30]Department of Pathology, Stanford University School of Medicine, Stanford, CA, USA. [31]Ludwig Center for Cancer Stem Cell Research and Medicine, Stanford University School of Medicine, Stanford, CA, USA. [32]Stanford Cancer Institute, Stanford University School of Medicine, Stanford, CA, USA. [33]Department of Medical Biotechnology, Faculty of Biochemistry, Biophysics and Biotechnology, Jagiellonian University, Krakow, Poland. [34]Wu Tsai Neurosciences Institute, Stanford University School of Medicine, Stanford, CA, USA. [35]Department of Electrical Engineering, Stanford University, Palo Alto, CA, USA. [36]Department of Epidemiology, Harvard T.H. Chan School of Public Health, Boston, MA, USA. [37]Department of Biomedical Data Science, Stanford University, Palo Alto, CA, USA. [38]Princess Máxima Center for Pediatric Oncology, Utrecht, The Netherlands. [39]School of Biomedical Engineering, University of British Columbia, Vancouver, British Columbia, Canada. [40]Department of Microbiology and Immunology, University of British Columbia, Vancouver, British Columbia, Canada. [41]Humans and the Microbiome Program, Canadian Institute for Advanced Research, Toronto, Ontario, Canada. ✉e-mail: spyros.darmanis@czbiohub.org; steve@quake-lab.org; twc@stanford.edu

Methods

All data, protocols, analysis scripts and an interactive data browser are publicly available.

Experimental procedures

Mice and organ collection. Male and virgin female C57BL/6JN mice were shipped from the National Institute on Ageing colony at Charles River (housed at 19–23 °C) to the Veterinary Medical Unit (VMU; housed at 20–24 °C)) at the VA Palo Alto (VA). At both locations, mice were housed on a 12 h/12 h light/dark cycle and provided with food and water ad libitum. The diet at Charles River was NIH-31, and at the VA VMU was Teklad 2918. Littermates were not recorded or tracked, and mice were housed at the VA VMU for no longer than 2 weeks before euthanasia, with the exception of mice older than 18 months, which were housed at the VA VMU beginning at 18 months of age. Before tissue collection, mice were placed in sterile collection chambers at 8:00 for 15 min to collect fresh fecal pellets. After anaesthetization with 2.5% v/v Avertin, mice were weighed, shaved, and blood was drawn via cardiac puncture before transcardial perfusion with 20 ml PBS. Mesenteric adipose tissue was then immediately collected to avoid exposure to the liver and pancreas perfusate, which negatively affects cell sorting. Isolating viable single cells from both the pancreas and the liver of the same mouse was not possible; therefore, two males and two females were used for each. Whole organs were then dissected in the following order: large intestine, spleen, thymus, trachea, tongue, brain, heart, lung, kidney, gonadal adipose tissue, bladder, diaphragm, limb muscle (tibialis anterior), skin (dorsal), subcutaneous adipose tissue (inguinal pad), mammary glands (fat pads 2, 3 and 4), brown adipose tissue (interscapular pad), aorta and bone marrow (spine and limb bones). Organ collection concluded by 10:00. After single-cell dissociation as described below, cell suspensions were used either for FACS of individual cells into 384-well plates, or for preparation of the microfluidic droplet library. All animal care and procedures were carried out in accordance with institutional guidelines approved by the VA Palo Alto Committee on Animal Research.

Tissue dissociation and sample preparation. All tissues were processed as previously described[5].

Sample size, randomization and blinding. No sample size choice was performed before the study. Randomization and blinding were not performed: the authors were aware of all data and metadata-related variables during the entire course of the study.

Single-cell methods. All protocols used in this study are described in detail elsewhere[5]. These include: preparation of lysis plates; FACS sorting; cDNA synthesis using the Smart-seq2 protocol[52,53]; library preparation using an in-house version of Tn5[54,55]; library pooling and quality control; and sequencing. For further details please refer to https://doi.org/10.17504/protocols.io.2uwgexe.

Microfluidic droplet single-cell analysis. Single cells were captured in droplet emulsions using the GemCode Single-Cell Instrument (10x Genomics) and scRNA-seq libraries were constructed as per the 10x Genomics protocol using GemCode Single-Cell 3′ Gel Bead and Library V2 Kit. In brief, single cell suspensions were examined using an inverted microscope, and if sample quality was deemed satisfactory, the sample was diluted in PBS with 2% FBS to a concentration of 1,000 cells per µl. If cell suspensions contained cell aggregates or debris, two additional washes in PBS with 2% FBS at 300*g* for 5 min at 4 °C were performed. Cell concentration was measured either with a Moxi GO II (Orflo Technologies) or a haemocytometer. Cells were loaded in each channel with a target output of 5,000 cells per sample. All reactions were performed in the Biorad C1000 Touch Thermal cycler with 96-Deep Well Reaction Module. Twelve cycles were used for cDNA amplification and sample index PCR. Amplified cDNA and final libraries were evaluated on a Fragment Analyzer using a High Sensitivity NGS Analysis Kit (Advanced Analytical). The average fragment length of 10x cDNA libraries was quantitated on a Fragment Analyzer (AATI), and by qPCR with the Kapa Library Quantification kit for Illumina. Each library was diluted to 2 nM, and equal volumes of 16 libraries were pooled for each NovaSeq sequencing run. Pools were sequenced with 100 cycle run kits with 26 bases for Read 1, 8 bases for Index 1, and 90 bases for Read 2 (Illumina 20012862). A PhiX control library was spiked in at 0.2 to 1%. Libraries were sequenced on the NovaSeq 6000 Sequencing System (Illumina).

In situ RNA hybridization and quantification. In situ RNA hybridization was performed using the Advanced Cell Diagnostics RNAscope Multiplex Fluorescent Detection kit v2 (323110, Bio-Techne) according to the manufacturer's instructions. Staining of mouse liver specimens was performed using 5-µm paraffin-embedded thick sessions. Mouse livers were fixed in 10% formalin buffer saline (HT501128, Sigma-Aldrich) for 24 h at room temperature before paraffin embedding. For multiplex staining the following probes were used; *Clec4f* (*Mm*-Clec4f 480421, *Il1b* (*Mm*-Il1b 316891-C2), *Pecam1* (*Mm*-Pecam-1 316721), *Mrc1* (*Mm*-Mrc1 437511-C3). Slides were counterstained with Prolong gold antifade reagent with DAPI (P36931, Life Technologies). Mounted slides were imaged on a Leica DM6 B fluorescent microscope (Leica Biosystems). Image quantification was performed using the starfish open source image-based transcriptomics pipeline (see Starfish: Open Source Image Based Transcriptomics and Proteomics Tools, available from http://github.com/spacetx/starfish and ref. [58]).

Computational methods

Data extraction. Sequences from the NovaSeq were de-multiplexed using bcl2fastq v.2.19.0.316. Reads were aligned to the mm10plus genome using STAR v.2.5.2b with parameters TK. Gene counts were produced using HTSEQ v.0.6.1p1 with default parameters, except 'stranded' was set to 'false', and 'mode' was set to 'intersection-nonempty'. Sequences from the microfluidic droplet platform were de-multiplexed and aligned using CellRanger v.2.0.1, available from 10x Genomics with default parameters.

Data pre-processing. Gene count tables were combined with the metadata variables using the Scanpy[56] Python package v.1.4.2. We removed genes that were not expressed in at least 3 cells and then cells that did not have at least 250 detected genes. For FACS we removed cells with fewer than 5,000 counts, and for the droplet method we removed cells with fewer than 2,500 unique molecular identifiers (UMIs). The data was then normalized using size factor normalization such that every cell has 10,000 counts and log transformed. We computed highly variable genes using default parameters and then scaled the data to a maximum value of 10. We then computed principal component analysis, neighbourhood graph and clustered the data using Louvain[7] and Leiden[8] methods. The data was visualized using UMAP projection. When performing batch correction to remove the technical artefacts introduced by the technologies, we replaced the neighbourhood graph computation with bbknn[6]. Step-by-step instructions to reproduce the pre-processing of the data are available from GitHub.

Cell type annotation. To define cell types we analysed each organ independently but combining all ages. In brief, we performed principal component analysis on the most variable genes between cells, followed by Louvain and Leiden graph-based clustering. Next we subset the data for 3 months (*Tabula Muris*[5]) and computed how many cell types map to each individual cluster. For the clusters that had a single 1:1 mapping (cluster:cell type) we propagated the annotations for all ages; in case there is a 1:many mapping we flagged that cluster for manual validation. Step-by-step instructions to reproduce this method are available

from GitHub. For each cluster, we provide annotations in the controlled vocabulary of the cell ontology[57] to facilitate inter-experiment comparisons. Using this method, we were able to annotate automatically (around 1 min per tissue) more than 70% of the dataset. The automatic annotations were then reviewed by each of the tissue experts leading to a fully curated dataset for all the cell types in the *Tabula Muris Senis*.

Tissue cell composition analysis. For each tissue and age, we computed the relative proportion of each cell type. Next we used scipy.stats linregress to regress the relative tissue-cell type changes against age and considered significant the changes with $P < 0.05$ for a hypothesis test with the null hypothesis that the slope is zero, using two-sided Wald test with t-distribution of the test statistic and a $r^2 > 0.5$.

Differential gene expression. We performed differential gene expression analysis on each tissue with a well-powered sample size (more than 100 cells in both young (1 month and 3 month) and old (18 months, 21 months, 24 months and 30 months) age groups). We used a linear model[51] treating age as a numerical variable while controlling for sex and technology. We applied a false-discovery rate (FDR) threshold of 0.01 and an age coefficient threshold of 0.005 (corresponding to an approximately 10% fold change).

Comparison between bulk and single-cell datasets. The differential gene analysis was defined on a per tissue basis. First, we investigated genes on the basis of the single-cell data. We considered only cells from male mice and perform our analysis on the log (1 + counts per million (cpm)) transformed single-cell count matrices. Note that normalization of the single-cell data was done on a per cell basis. We defined two groups of cells on the basis of age: young cells with age ≤ 3 months (Y) and old cells with age >3 months (O). For each gene we compute the $\log_2$ fold change of cell and read counts between O and Y. We defined cell count as the fraction of cells that express the gene. Similarly, we defined read count as the mean read count of the gene in the cells that express it. The calculated $\log_2$ fold-changes of a gene reflect its expression changes with ageing within the single-cell data. Next we analysed each gene on the basis of the bulk data. We computed the Spearman correlation (ρ) of bulk DESeq2 normalized gene expression with ageing. We defined two groups of genes on the basis of the bulk data, increasing with age $\rho > 0.7$ (U) and decreasing with age $\rho < -0.7$ (D). Finally, we compared the $\log_2$ fold-changes based on the single-cell data between the bulk data defined groups U and D. Specifically, we ran a Wilcoxon–Mann–Whitney test to understand whether $\log_2$ fold-changes of cell or read counts could distinguish between the two groups. We used the U statistic for effect size.

T cell processing. We used TraCeR[44] v.0.5 to identify T cell clonal populations. We ran tracer assemble with–species Mmus set. We then ran tracer summarize with –species Mmus to create the final results. We used the following versions for TraCeR dependencies: igblast v.1.7.0, kallisto v.0.43.1, Salmon v.0.8.2, Trinity v.2.4.0, GRCm38 reference genome. Step-by-step instructions to reproduce the processing of the data are available from GitHub.

B cell processing. We used singlecell-ige[43] v.eafb6d126cc2d6511faae3efbd442abd7c6dc8ef (https://github.com/dcroote/singlecell-ige) to identify B cell clonal populations. We used the default configuration settings, except we set the species to mouse. Step-by-step instructions to reproduce the processing of the data are available from GitHub.

Mutation analysis. We used samtools[59] v.1.9 and GATK[39] v.4.1.1.0 for mutation analysis. We used samtools faidx to create our index file. Then we used GATK CreateSequenceDictionary and GRCm38, as the reference, to create our sequence dictionary. Next we used GATK AddOrReplaceReadGroups to create a single read group using parameters -RGID 4 -RGLB lib1 -RGPL illumina -RGPU unit1 -RGSM 20. Finally we used GATK HaplotypeCaller to call the mutations. We disabled the following read filters: MappingQualityReadFilter, GoodCigarReadFilter, NotSecondaryAlignmentReadFilter, MappedReadFilter, MappingQualityAvailableReadFilter, Non-zeroReferenceLengthAlignmentReadFilter, NotDuplicateReadFilter, PassesVendorQualityCheckReadFilter, and WellformedReadFilter, but kept all other default settings. The results were summarized per gene in the form of a mutation count per cell table. We started by removing genes mutated in more than 60% of cells, to eliminate the possible bias of germline mutations. Then for each tissue we selected genes expressed in at least 75% of the cells for all the time points to avoid confounding the mutation results with differential gene expression associated with age. Next we computed the average number of mutations in the gene set (or ERCC spike-in controls) per cell and also the average number of raw counts (Supplementary Table 8) and plotted the different distributions. Step-by-step instructions to reproduce the processing of the data are available from GitHub.

Trajectory analysis. We used partition-based graph abstraction (PAGA[60]) to reconstruct the ageing trajectory in brain microglial cells. Step-by-step instructions to reproduce the processing of the data are available from GitHub.

Diversity score. The raw FACS or droplet dataset were used as the input. We filtered genes expressed in fewer than 5 cells, filtered cells if expressing fewer than 500 genes and discarded cells with total number of counts less than 5,000. Next we performed size factor normalization such that every cell had 1×10^4 counts and performed a log1p transformation. This was followed by clustering, in which we clustered every tissue and every tissue-cell type for every mouse separately using 6 different configurations: resolution parameters (0.3, 0.5, 0.7) × clustering method (Louvain, Leiden). This is to provide a robust clustering result. For each combination (each tissue–mouse and each tissue–cell_type–mouse), we computed the clustering diversity score as the Shannon entropy of the cluster assignment. We then regressed the diversity score against age to detect the systematic increase or decrease of clustering diversity with respect to age. FDR was used to correct for multiple comparisons. A tissue or a tissue–cell type was selected if the slope was consistent (having the same sign) in all six clustering configurations and at least two out of six clustering configurations had FDR <0.3. For each selected tissue or tissue–cell type, a separate UMAP was computed using cells from all mice for visualization using Leiden clustering with resolution parameter 0.7.

Reporting summary

Further information on research design is available in the Nature Research Reporting Summary linked to this paper.

Data availability

The entire dataset can be explored interactively at http://tabula-muris-senis.ds.czbiohub.org/. Gene counts and metadata are available from figshare (https://doi.org/10.6084/m9.figshare.8273102.v2) and the Gene Expression Omnibus under accession code GSE132042; the raw data files are available from a public AWS S3 bucket (https://registry.opendata.aws/tabula-muris-senis/).

Code availability

The code used for the analysis is available from GitHub at https://github.com/czbiohub/tabula-muris-senis.

52. Picelli, S. et al. Smart-seq2 for sensitive full-length transcriptome profiling in single cells. *Nat. Methods* **10**, 1096–1098 (2013).
53. Darmanis, S. et al. A survey of human brain transcriptome diversity at the single cell level. *Proc. Natl Acad. Sci. USA* **112**, 7285–7290 (2015).

54. Picelli, S. et al. Tn5 transposase and tagmentation procedures for massively scaled sequencing projects. *Genome Res*. **24**, 2033–2040 (2014).
55. Hennig, B. P. et al. Large-scale low-cost NGS library preparation using a robust Tn5 purification and tagmentation protocol. *G3 (Bethesda)* **8**, 79–89 (2018).
56. Wolf, F. A., Angerer, P. & Theis, F. J. SCANPY: large-scale single-cell gene expression data analysis. *Genome Biol*. **19**, 15 (2018).
57. Diehl, A. D. et al. The Cell Ontology 2016: enhanced content, modularization, and ontology interoperability. *J. Biomed. Semantics* **7**, 44 (2016).
58. McQuin, C. et al. CellProfiler 3.0: Next-generation image processing for biology. *PLoS Biol*. **16**, e2005970 (2018).
59. Li, H. et al. The Sequence Alignment/Map format and SAMtools. *Bioinformatics* **25**, 2078–2079 (2009).
60. Wolf, F. A. et al. PAGA: graph abstraction reconciles clustering with trajectory inference through a topology preserving map of single cells. *Genome Biol*. **20**, 59 (2019).

Acknowledgements We thank Sony Biotechnology for making an SH800S instrument available for this project. Some of the cell sorting and flow cytometry analysis for this project was done on a Sony SH800S instrument in the Stanford Shared FACS Facility. Some FACS experiments were performed with instruments in the VA Flow Cytometry Core, which is supported by the US Department of Veterans Affairs (VA), Palo Alto Veterans Institute for Research (PAVIR), and the National Institutes of Health (NIH). This work was supported by the Chan Zuckerberg Biohub, Department of Veterans Affairs grant IK6 BX004599 (T.W.-C.) and NIH/NIA DP1 grant AG053015 (T.W.-C.). We thank B. Tojo for the artwork, and C. Xu and J. Batson for discussions.

Author contributions A full list of author contributions can be found in the Supplementary Information.

Competing interests The authors declare no competing interests.

Additional information
Supplementary information is available for this paper at https://doi.org/10.1038/s41586-020-2496-1.
Correspondence and requests for materials should be addressed to S.D., S.R.Q. or T.W.-C.
Peer review information *Nature* thanks Fan Zhang and the other, anonymous, reviewer(s) for their contribution to the peer review of this work.

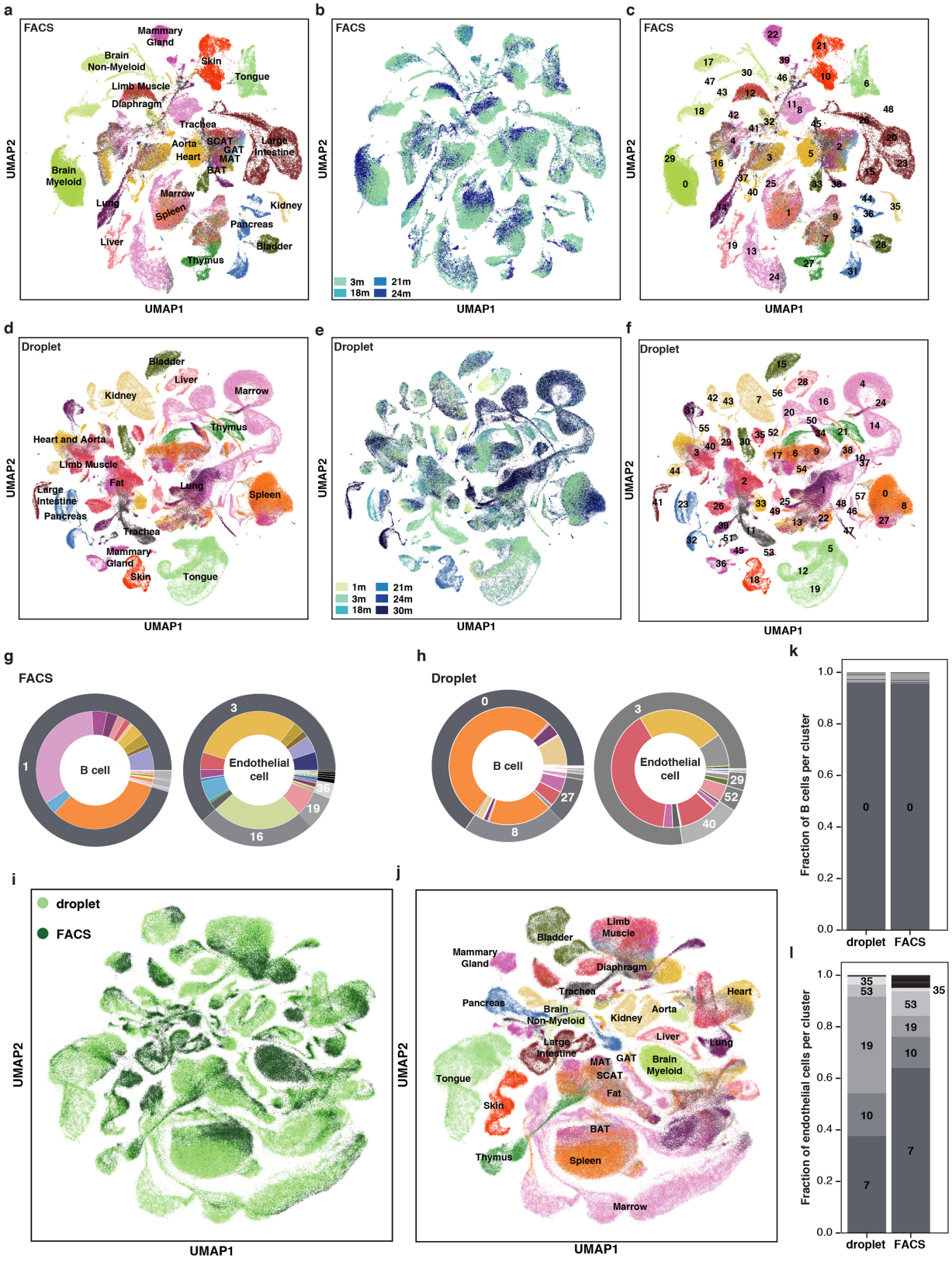

Extended Data Fig. 1 | See next page for caption.

Extended Data Fig. 1 | UMAP visualizations of the whole *Tabula Muris Senis*. **a**, **b**, UMAP plot of all cells collected for FACS coloured by tissue (**a**) or age (**b**). **c**, UMAP plot of all cells collected by FACS, coloured by organ (Extended Data Fig. 4c), overlaid with the Louvain cluster numbers. $n = 110{,}824$ individual cells for FACS. **d**, **e**, UMAP plot of all cells collected for droplet coloured by tissue (**d**) or age (**e**). **f**, UMAP plot of all cells collected by droplet, coloured by organ (Extended Data Fig. 4c), overlaid with the Louvain cluster numbers. $n = 245{,}389$ individual cells for droplet. **g**, B cells (left) and endothelial cells (right) in FACS independently annotated for each organ cluster together by unbiased whole-transcriptome Louvain clustering, irrespective of the organ from which they originated. **h**, B cells (left) and endothelial cells (right) in droplet independently annotated for each organ cluster together by unbiased whole-transcriptome Louvain clustering, irrespective of the organ from which they originated. **i**, **j**, UMAP plot of all cells collected coloured by method (**i**) or tissue (**j**). $n = 356{,}213$ individual cells for FACS and droplet combined. **k**, **l**, B cells (**k**) and endothelial cells (**l**) cluster together by unbiased whole-transcriptome Louvain clustering, irrespective of the technology by which they were found.

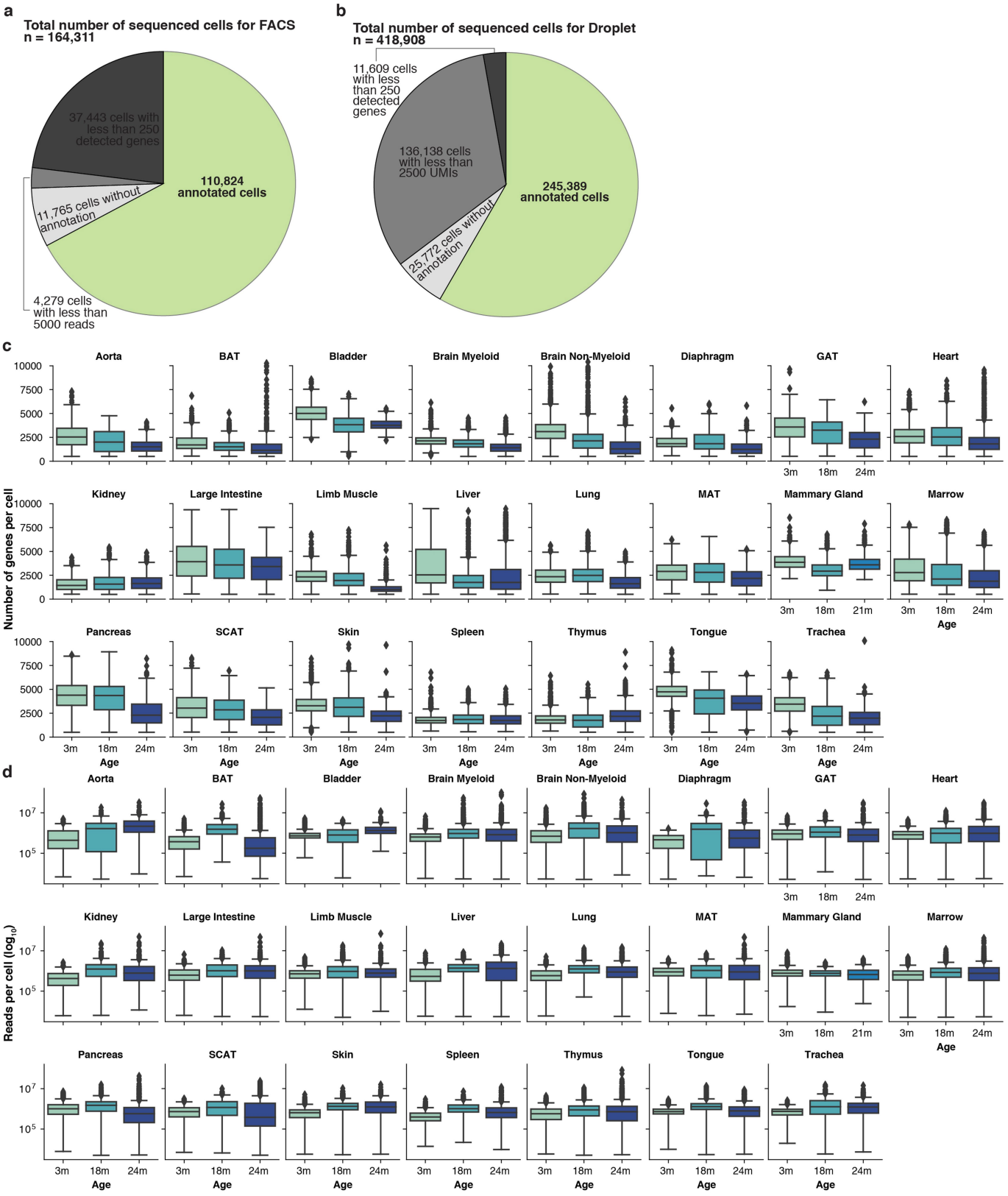

Extended Data Fig. 2 | *Tabula Muris Senis* quality control statistics overall summary and detailed for the FACS dataset. a, Pie chart with the summary statistics for FACS. **b**, Pie chart with the summary statistics for droplet. **c**, Box plot of the number of genes detected per cell for each organ and age for FACS. **d**, Box plot of the number of reads per cell (log-scale) for each organ and age for FACS. For **c**, **d**, all data are expressed as mean ± s.d. Individual data points (black diamonds) correspond to outliers outside of the quantile distribution. The sample size (number of cells for each tissue and age) is available in Supplementary Table 1.

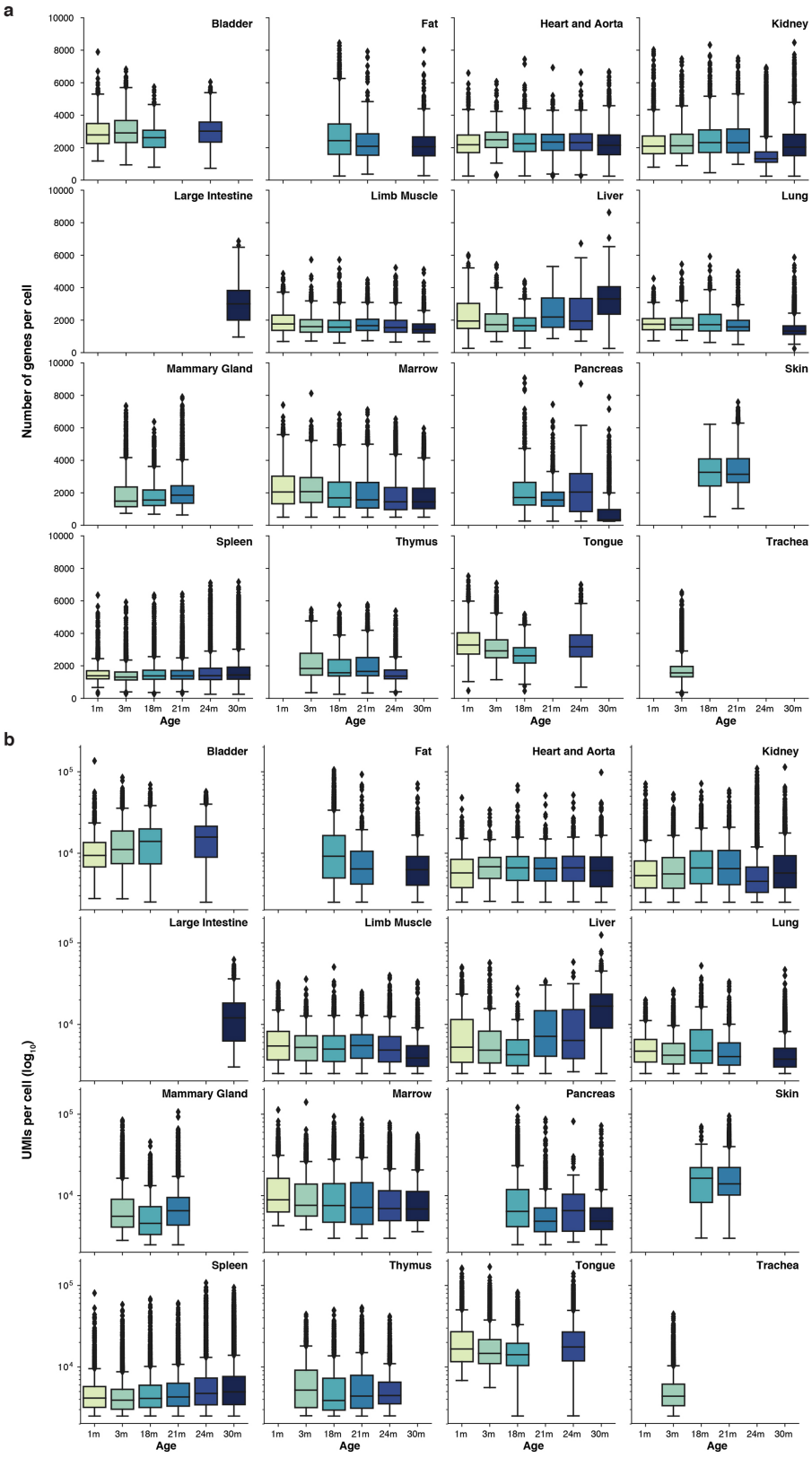

Extended Data Fig. 3 | *Tabula Muris Senis* quality control statistics detailed for the droplet dataset. a, Box plot of the number of genes detected per cell for each organ and age for droplet. **b**, Box plot of the number of UMIs per cell (log scale) for each organ and age for droplet. All data are expressed as mean ± s.d. Individual data points (black diamonds) correspond to outliers outside of the quantile distribution. The sample size (number of cells for each tissue and age) is available in Supplementary Table 2.

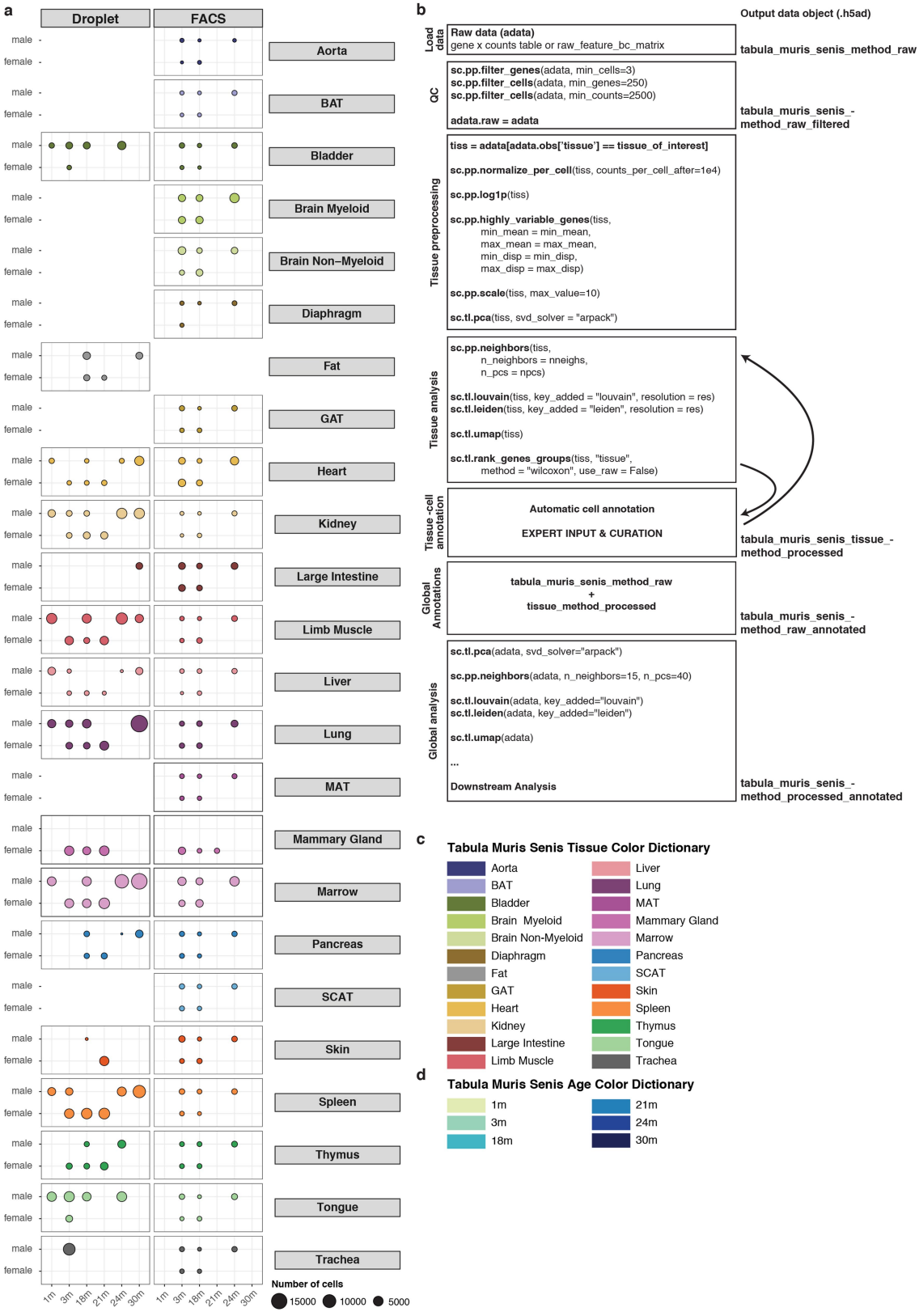

Extended Data Fig. 4 | Number of cells in Tabula Muris Senis across age, sex, tissue and technology and schematic the of data processing. a, Balloon plot showing the number of sequenced cells per sequencing method per organ per sex per age. **b**, Schematic of the analysis workflow. **c**, **d**, *Tabula Muris Senis* colour dictionary for organs and tissues (**c**) and ages (**d**).

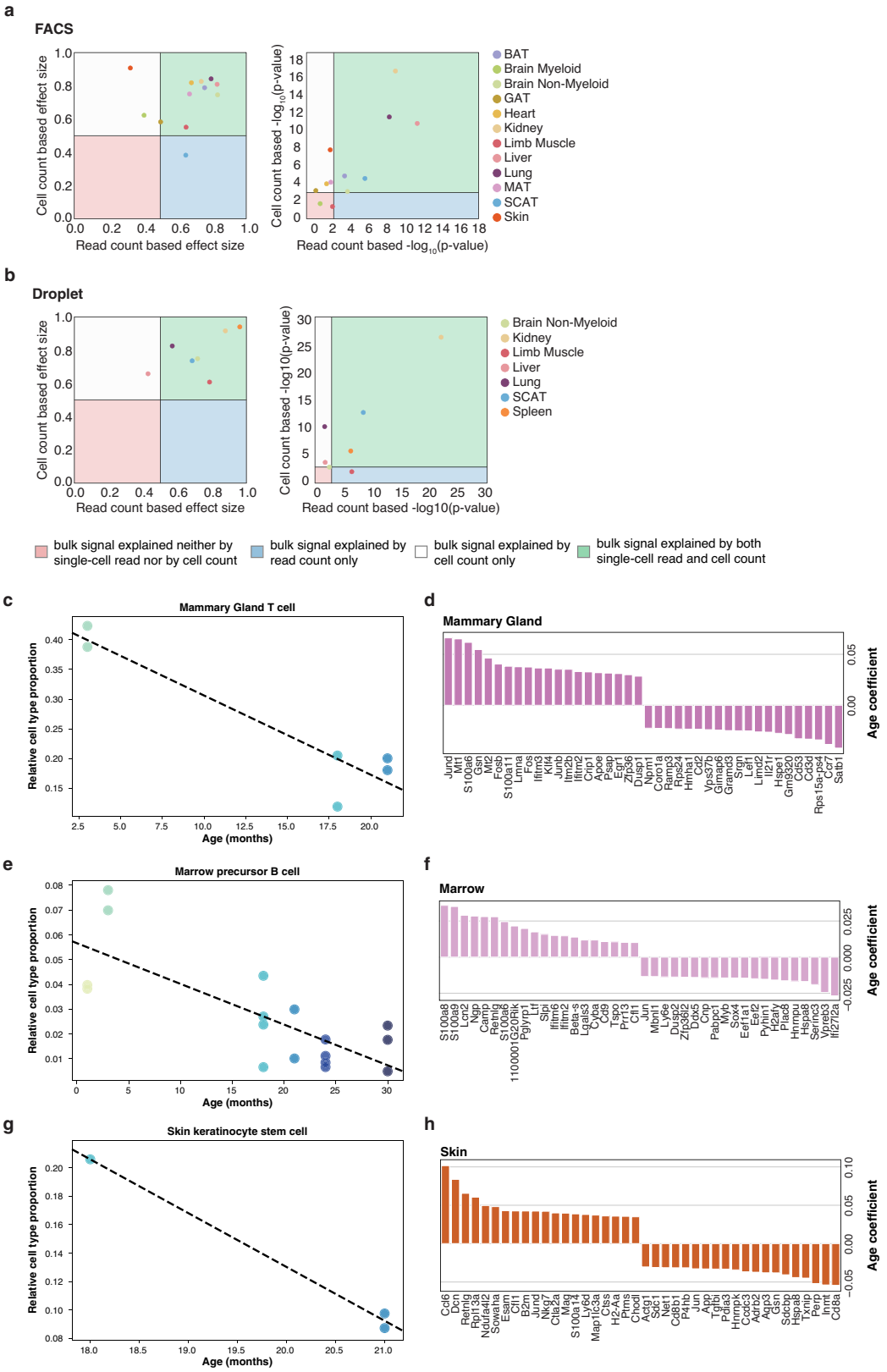

Extended Data Fig. 5 | See next page for caption.

Extended Data Fig. 5 | Comparison of bulk and single-cell datasets and tissue cell compositions. a, **b**, Ageing patterns from bulk and single-cell data are consistent. Strong changes in bulk gene expression with ageing can be either explained by cell or read count-based changes in single-cell data FACS (**a**) and droplet (**b**). Two-sided Wilcoxon–Mann–Whitney indicates that single-cell data based $\log_2$ fold-changes of cell or read counts distinguish between up and down regulated genes in bulk data. $n = 110{,}824$ individual cells for FACS and $n = 245{,}389$ individual cells for droplet. **c**, Mammary gland T cell relative abundances change significantly with age ($P < 0.05$ and $r^2 > 0.7$ for a hypothesis test with the null hypothesis that the slope is zero, using two-sided Wald test with *t*-distribution of the test statistic). **d**, Top 20 upregulated and downregulated genes in mammary gland computed using MAST[51], treating age as a continuous covariate while controlling for sex and technology. Genes were classified as significant under an FDR threshold of 0.01 and an age coefficient threshold of 0.005 (corresponding to an approximately 10% fold change). $n = 6{,}393$, 3,635 and 5,549 individual cells for mammary gland at 3, 18 and 21 months, respectively. **e**, Relative abundances of marrow precursor B cells change significantly with age ($P < 0.05$ and $r^2 > 0.7$ for a hypothesis test with the null hypothesis that the slope is zero, using two-sided Wald test with *t*-distribution of the test statistic). **f**, Top 20 upregulated and downregulated genes in marrow computed using MAST[51], treating age as a continuous covariate while controlling for sex and technology. Genes were classified as significant under an FDR threshold of 0.01 and an age coefficient threshold of 0.005 (corresponding to an approximately 10% fold change). $n = 3{,}027$, 8,559, 11,496, 5,216, 12,943 and 13,496 individual cells for marrow at 1, 3, 18, 21, 24 and 30 months, respectively. **g**, Relative abundances of skin keratinocyte stem cells change significantly with age ($P < 0.05$ and $r^2 > 0.7$ for a hypothesis test with the null hypothesis that the slope is zero, using two-sided Wald test with *t*-distribution of the test statistic). **h**, Top 20 upregulated and downregulated genes in skin computed using MAST[51], treating age as a continuous covariate while controlling for sex and technology. Genes were classified as significant under an FDR threshold of 0.01 and an age coefficient threshold of 0.005 (corresponding to an approximately 10% fold change). $n = 2{,}346$, 1,494, 4,352 and 1,122 individual cells for skin at 3, 18, 21 and 24 months, respectively. The *P* values for the cell type compositional changes are shown in Supplementary Table 5.

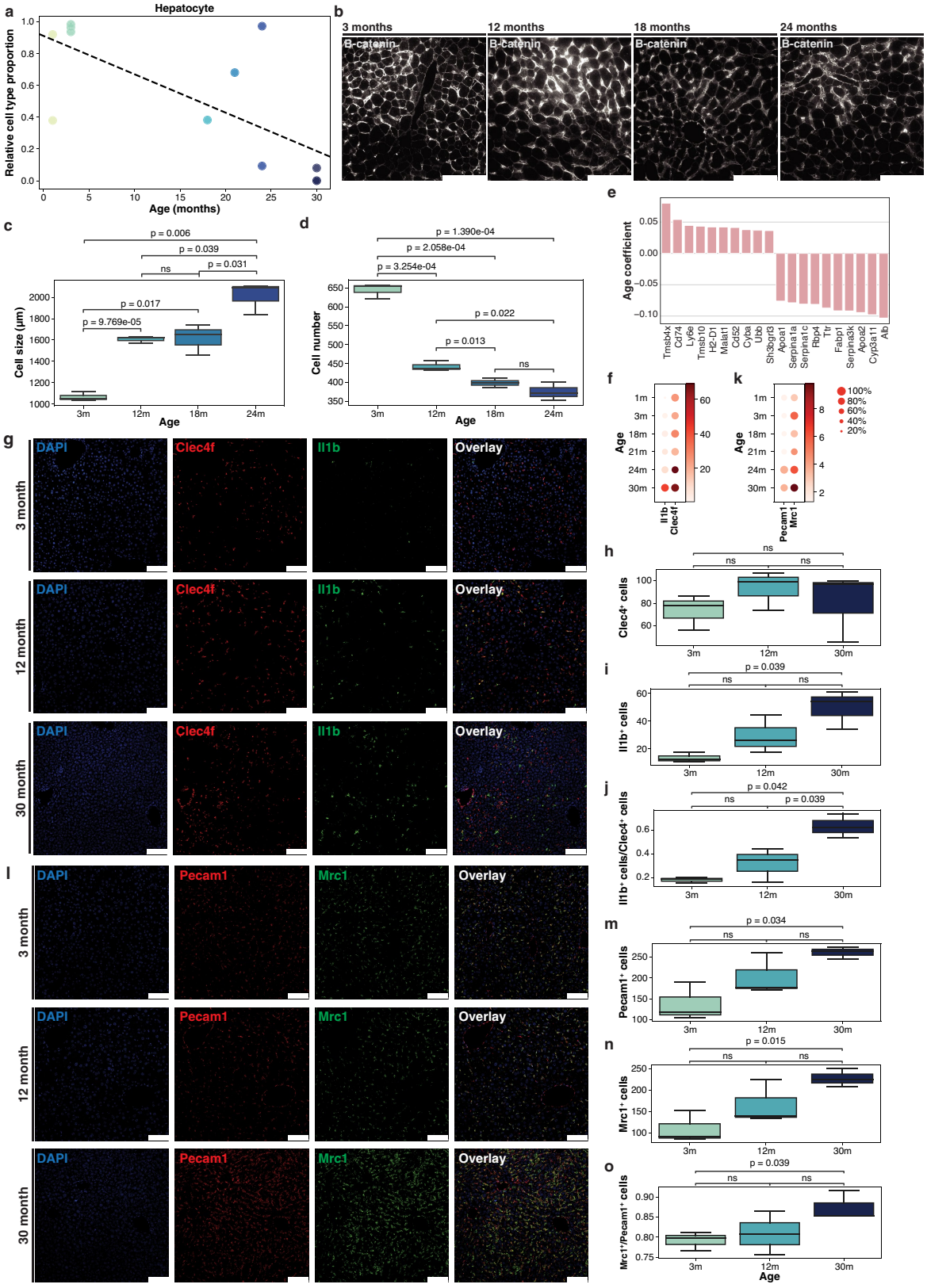

Extended Data Fig. 6 | See next page for caption.

Extended Data Fig. 6 | Cellular changes during ageing in the liver. a, Relative abundances of liver hepatocytes change significantly with age ($P < 0.05$ and $r^2 > 0.7$ for a hypothesis test with the null hypothesis that the slope is zero, using two-sided Wald test with *t*-distribution of the test statistic). $n = 2{,}791$, 2,832, 3,806, 2,257, 6,384 and 5,713 individual cells for liver 1, 3, 18, 21, 24 and 30 months, respectively. The *P* values for the cell type compositional changes are shown in Supplementary Table 5. **b**–**d**, Bright-field imaging of hepatocytes at different ages (**b**) and respective quantification (**c**, **d**). **e**, Top 10 upregulated and downregulated genes in liver computed using MAST[51], treating age as a continuous covariate while controlling for sex and technology. Genes were classified as significant under an FDR threshold of 0.01 and an age coefficient threshold of 0.005 (corresponding to an approximately 10% fold change). The sample size is the same as for **a**. **f**, **k**, Gene expression of *Il1b* and *Clec4f* (**f**) and *Pecam1* and *Mrc1* (**k**) in the liver droplet dataset for the six ages. **g**–**j**, Staining of Kupffer cells at different ages (**g**) and respective quantification (**h**–**j**). **l**–**o**, Staining of liver endothelial cells at different ages (**l**) and respective quantification (**m**–**o**). Scale bars, 100 µm. For **c**, **d**, **h**–**j** and **m**–**o**, all data are expressed as mean ± s.d. and *P* values were obtained using a Welch's test. The sample size for each group is available in Supplementary Table 7.

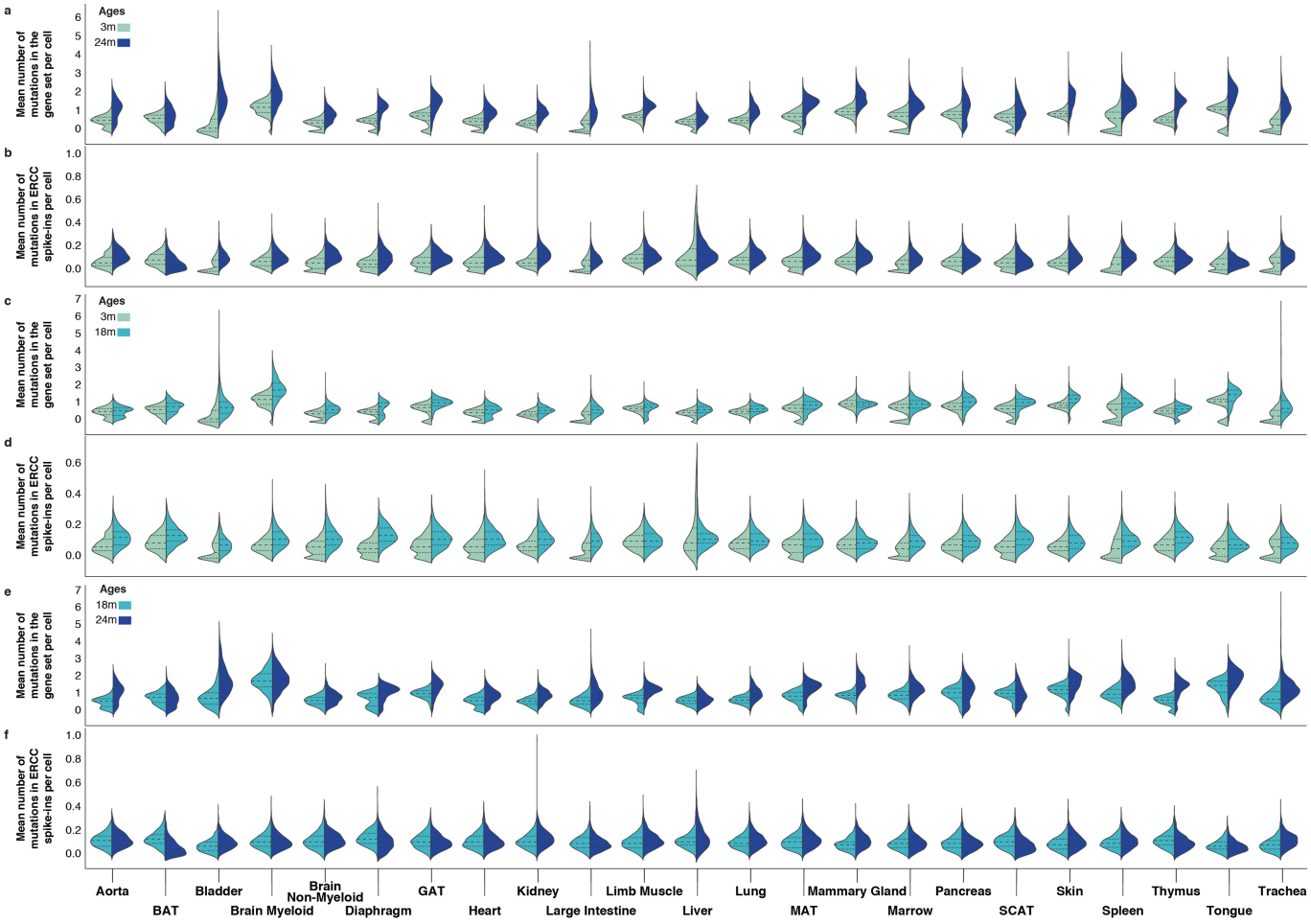

Extended Data Fig. 7 | Mean number of somatic mutations with age. **a**–**f**, Mean number of somatic mutations in genes (**a**, **c**, **e**) and ERCC spike-in controls (**b**, **d**, **f**) across all tissues per age group (3 months and 24 months (**a**, **b**), 3 months and 18 months (**c**, **d**), 18 months and 24 months (**e**, **f**)). Mutations are presented as the mean number of mutations per gene or ERCC spike-in per cell.

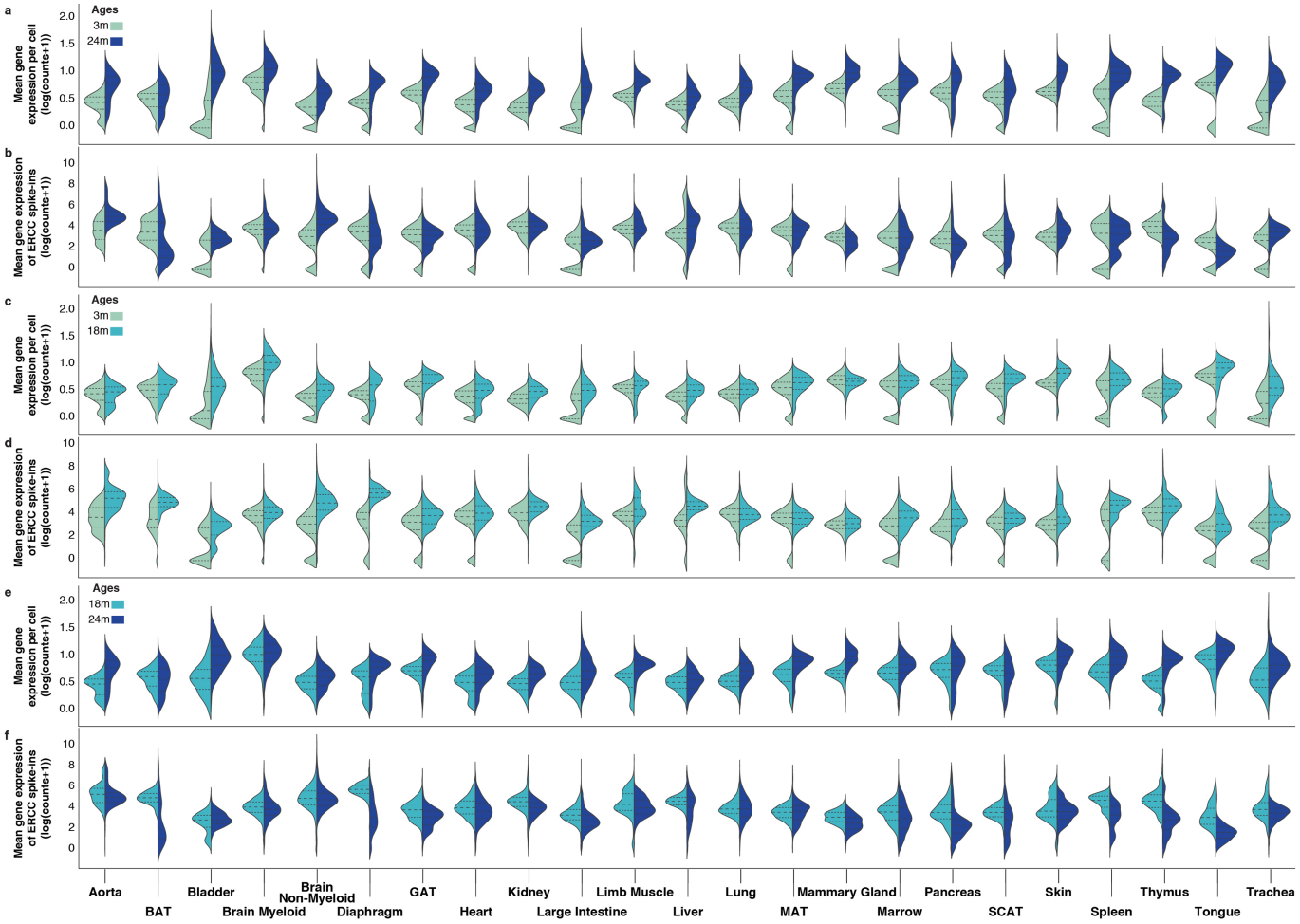

Extended Data Fig. 8 | Gene (raw) expression with age. a–**f**, Gene raw expression (**a**, **c**, **e**) and ERCC spike-in control raw expression (**b**, **d**, **f**) across all tissues per age group (3 months and 24 months (**a**, **b**), 3 months and 18 months (**b**, **d**), 18 months and 24 months (**c**, **e**)). Raw expression are presented as the mean number of counts per gene or ERCC spike-inn control per cell.

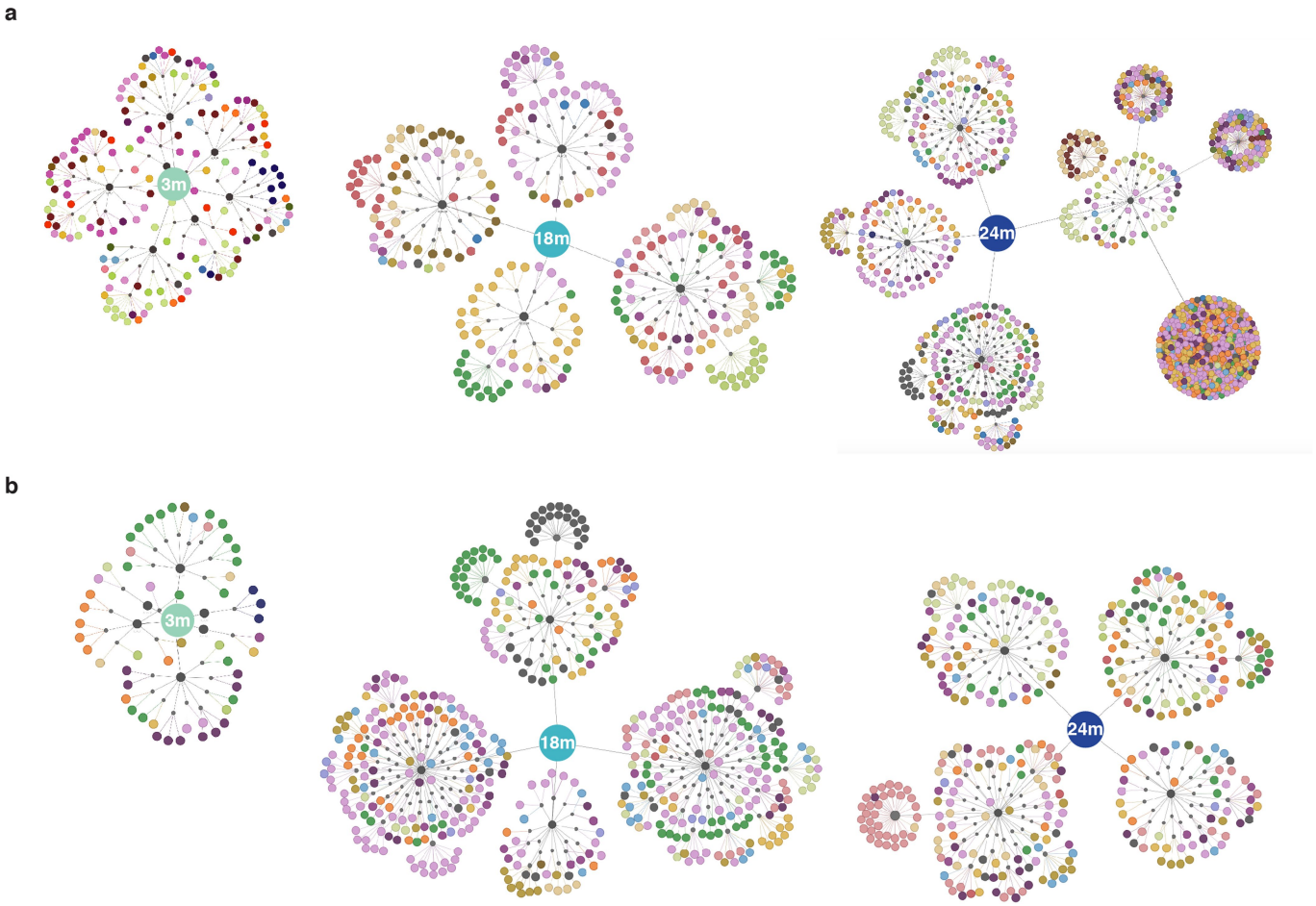

Extended Data Fig. 9 | Immune repertoire clonality analysis. a, B-cell clonal families. For each time point, the clonal families are represented in a tree structure for which the central node is age. Connected to the age node there is an additional node (dark grey) that represents each mouse and the clonal families are depicted for each mouse. For each clonal family, cells that are part of that family are coloured by the organ of origin. **b**, T-cell clonal families. For each time point, clonal families are represented in a tree structure for which the central node is age. Connected to the age node there is an additional node (dark grey) that represents each mouse and the clonal families are depicted for each mouse. For each clonal family, cells that are part of that family are coloured by the organ of origin.

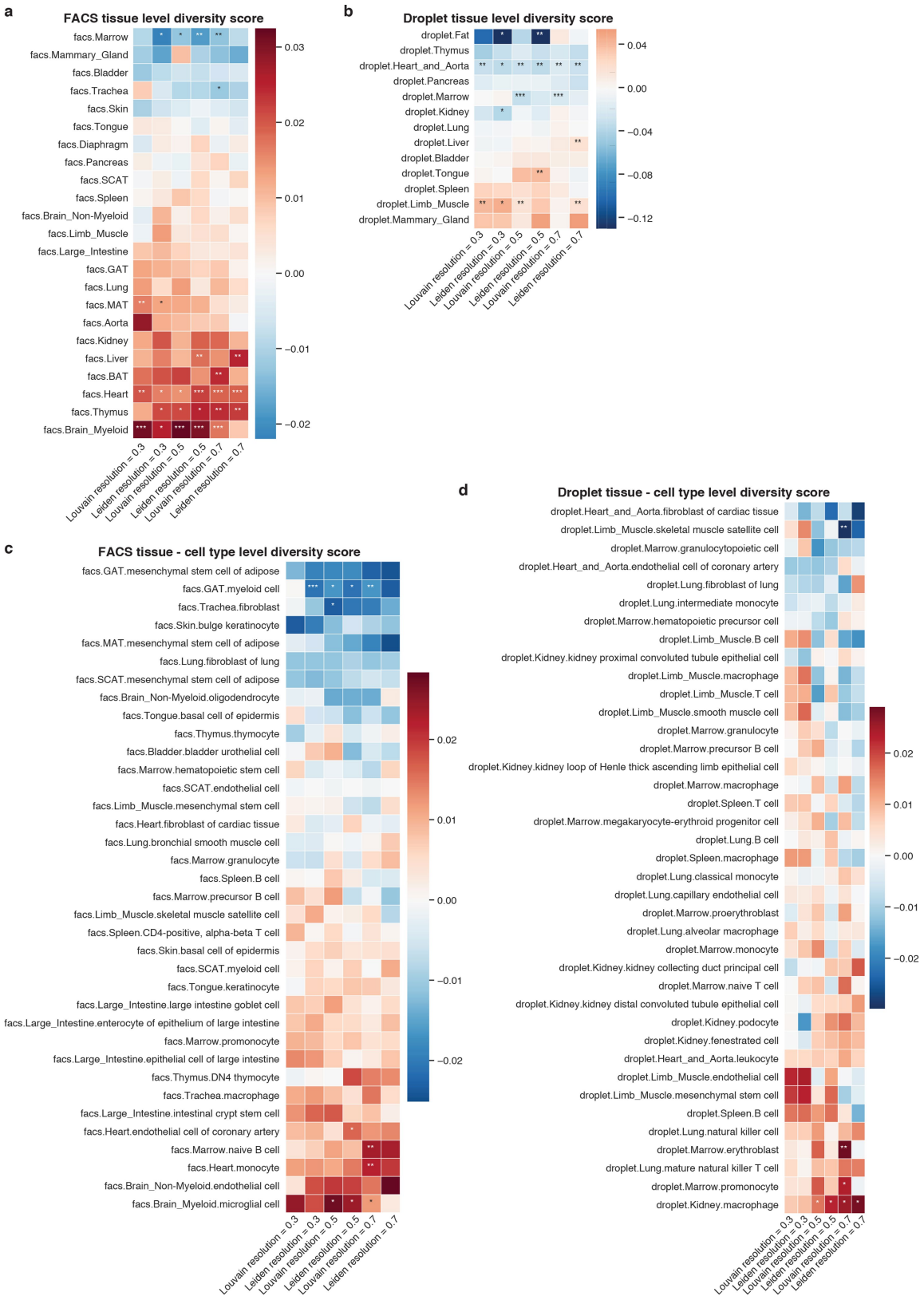

Extended Data Fig. 10 | Diversity score summary. a, **b**, Heat map summary of the overall tissue diversity score for FACS (**a**) and droplet (**b**). **c**, **d**, Heat map summary of the tissue cell-type diversity score for FACS (**c**) and droplet (**d**).

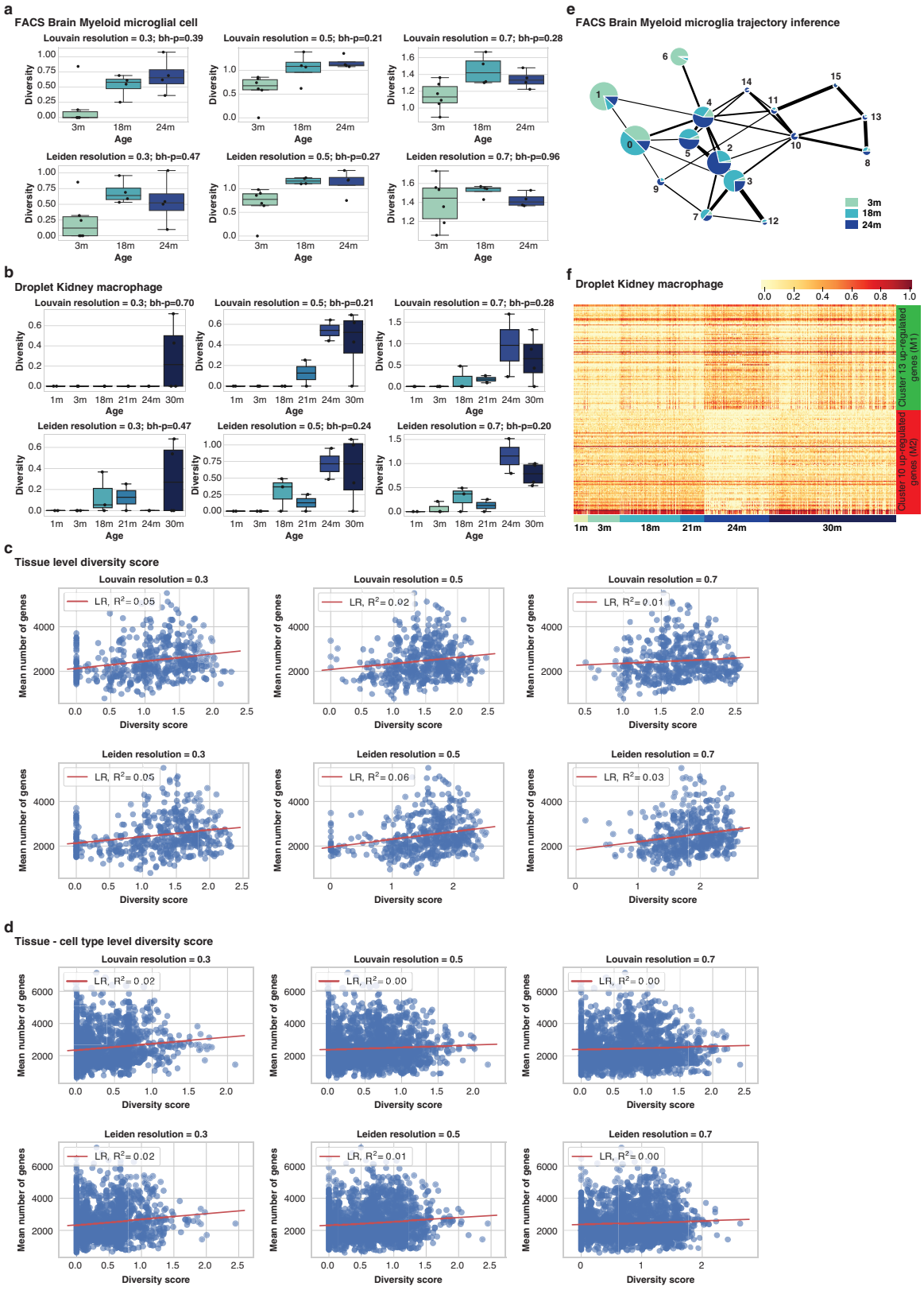

Extended Data Fig. 11 | Diversity score and differential gene expression analysis for brain myeloid and kidney. a, **b**, Diversity score at different cluster resolutions for FACS brain myeloid microglia cell (**a**) and droplet kidney macrophage (**b**). $n = 14$ mice for **a** and $n = 16$ mice for **b**. All data are expressed as quantiles. The P values were obtained using a linear regression and two-sided F-test, adjusted for multiple comparison using the Benjamini–Hochberg procedure (that is, bh-p value). **c**, **d**, Diversity score correlation with the number of genes expressed per tissue (**c**) or tissue cell-type (**d**). The red line corresponds to the linear regression curve. **e**, Trajectory analysis for a brain myeloid microglia cell. **f**, Heat map showing differential gene expression analysis of cluster 10 (mostly young macrophages) compared with cluster 13 (mostly old macrophages). For the complete gene list, see Supplementary Table 10.

nature research

Corresponding author(s): Spyros Darmanis, Tony Wyss-Coray and Stephen R. Quake

Last updated by author(s): April 5, 2020

Reporting Summary

Nature Research wishes to improve the reproducibility of the work that we publish. This form provides structure for consistency and transparency in reporting. For further information on Nature Research policies, see Authors & Referees and the Editorial Policy Checklist.

Statistics

For all statistical analyses, confirm that the following items are present in the figure legend, table legend, main text, or Methods section.

n/a	Confirmed	
☐	☒	The exact sample size (*n*) for each experimental group/condition, given as a discrete number and unit of measurement
☐	☒	A statement on whether measurements were taken from distinct samples or whether the same sample was measured repeatedly
☐	☒	The statistical test(s) used AND whether they are one- or two-sided *Only common tests should be described solely by name; describe more complex techniques in the Methods section.*
☐	☒	A description of all covariates tested
☐	☒	A description of any assumptions or corrections, such as tests of normality and adjustment for multiple comparisons
☐	☒	A full description of the statistical parameters including central tendency (e.g. means) or other basic estimates (e.g. regression coefficient) AND variation (e.g. standard deviation) or associated estimates of uncertainty (e.g. confidence intervals)
☐	☒	For null hypothesis testing, the test statistic (e.g. *F*, *t*, *r*) with confidence intervals, effect sizes, degrees of freedom and *P* value noted *Give P values as exact values whenever suitable.*
☒	☐	For Bayesian analysis, information on the choice of priors and Markov chain Monte Carlo settings
☒	☐	For hierarchical and complex designs, identification of the appropriate level for tests and full reporting of outcomes
☒	☐	Estimates of effect sizes (e.g. Cohen's *d*, Pearson's *r*), indicating how they were calculated

Our web collection on statistics for biologists contains articles on many of the points above.

Software and code

Policy information about availability of computer code

Data collection	Sequences from the NovaSeq were de-multiplexed using bcl2fastq version 2.19.0.316. Reads were aligned using to the mm10plus genome using STAR version 2.5.2b with parameters TK. Gene counts were produced using HTSEQ version 0.6.1p1 with default parameters, except 'stranded' was set to 'false', and 'mode' was set to 'intersection-nonempty'. Sequences from the microfluidic droplet platform were de-multiplexed and aligned using CellRanger version 2.0.1, available from 10x Genomics with default parameters.
Data analysis	We used Python version 3.7, Scanpy v1.4.2, bbknn v1.3.9, Starfish v0.1.9, TraCeR v0.5, Salmon v0.8.2, Kallisto v0.43.1, and DESeq2 v1.26.0. Code is available from GitHub (https://github.com/czbiohub/tabula-muris-senis).

For manuscripts utilizing custom algorithms or software that are central to the research but not yet described in published literature, software must be made available to editors/reviewers. We strongly encourage code deposition in a community repository (e.g. GitHub). See the Nature Research guidelines for submitting code & software for further information.

Data

Policy information about availability of data

All manuscripts must include a data availability statement. This statement should provide the following information, where applicable:

- Accession codes, unique identifiers, or web links for publicly available datasets
- A list of figures that have associated raw data
- A description of any restrictions on data availability

The dataset can be explored interactively at tabula-muris-senis.ds.czbiohub.org. Gene counts, metadata and raw data are available from a public AWS S3 bucket (https://s3.console.aws.amazon.com/s3/buckets/czb-tabula-muris-senis/) and GEO GSE132042. All code is available from GitHub (https://github.com/czbiohub/tabula-muris-senis)

Field-specific reporting

Please select the one below that is the best fit for your research. If you are not sure, read the appropriate sections before making your selection.

☒ Life sciences ☐ Behavioural & social sciences ☐ Ecological, evolutionary & environmental sciences

For a reference copy of the document with all sections, see nature.com/documents/nr-reporting-summary-flat.pdf

Life sciences study design

All studies must disclose on these points even when the disclosure is negative.

Sample size	No sample size calculation was performed. The number of mice was chosen to include a minimum of 2 mice per age group. Regarding the number of cells, no prior sample size calculation was performed. The sample size varies for each organ, as documented in the supplemental text. This was due to experimental constraints, for example: conflicting tissue dissociation protocols for liver and pancreas which limited our ability to process single cells from both of these organs from the same animal. We have a total of 19 male and 11 female mice and the sample size varies for each organ, as documented in the supplemental text.
Data exclusions	Exclusion criteria were pre-establish: Cells with fewer than 500 detected genes were excluded. (A gene counts as detected if it has at least one read mapping to it). Cells with fewer than 50,000 reads (FACS) or 1000 UMI (microfluidic droplet) were excluded.
Replication	Besides the biological replicates included in the study, we have not replicated any findings
Randomization	Mice were randomized within their respective age groups. Two mice from each age group were randomly selected to be sacrificed on each collection day. In addition, given the grouping of mice across age groups and the fact that each age group was processed across several days we do not believe that further randomization is relevant.
Blinding	We did not have experimental groups in this study.

Reporting for specific materials, systems and methods

We require information from authors about some types of materials, experimental systems and methods used in many studies. Here, indicate whether each material, system or method listed is relevant to your study. If you are not sure if a list item applies to your research, read the appropriate section before selecting a response.

Materials & experimental systems

n/a	Involved in the study
☐	☒ Antibodies
☒	☐ Eukaryotic cell lines
☒	☐ Palaeontology
☐	☒ Animals and other organisms
☒	☐ Human research participants
☒	☐ Clinical data

Methods

n/a	Involved in the study
☒	☐ ChIP-seq
☐	☒ Flow cytometry
☒	☐ MRI-based neuroimaging

Antibodies

Antibodies used

Number;Antigen name;Fluorophore;Company;Cat No;Reactivity species;Origin species;Clonality;Clone;Application;Link
1;ACSA2;PE;Miltenyi;130102365;mouse;rat;monoclonal; IH3-18A3;IF, FC;https://www.miltenyibiotec.com/US-en/products/macs-flow-cytometry/antibodies/primary-antibodies/anti-acsa-2-antibodies-mouse-ih3-18a3-1-10.html/
2;rabbit IgG;AF488;Invitrogen;A11034;rabbit;goat;polyclonal;NA;IF, FC, IHC;https://www.thermofisher.com/antibody/product/Goat-anti-Rabbit-IgG-H-L-Highly-Cross-Adsorbed-Secondary-Antibody-Polyclonal/A-11034
3;Ter119;Pacific Blue;Biolegend;116232;mouse;rat;monoclonal;Ter-119;FC;https://www.biolegend.com/en-us/products/pacific-blue-anti-mouse-ter-119-erythroid-cells-antibody-6137
4;CD45R/B220;FITC;BioLegend;103206;mouse,human,cat;rat;monoclonal; RA3-6B2;FC;https://www.biolegend.com/en-us/products/fitc-anti-mouse-human-cd45r-b220-antibody-445
5;CD106;PE/Cy7;BioLegend;105720;mouse;rat;monoclonal; 429 (MVCAM.A);FC;https://www.biolegend.com/en-us/products/pe-cy7-anti-mouse-cd106-antibody-6135
6;CD11B/MAC1;FITC;BioLegend;101206;mouse, human, chimpanzee, baboon, cynomolgus, rhesus, rabbit;rat;monoclonal; M1/70;FC;https://www.biolegend.com/en-us/products/fitc-anti-mouse-human-cd11b-antibody-347
7;anti-mouse Lineage Cocktail;FITC;BioLegend;133301;mouse;Armenian Hamster, rat;mixture of monoclonals;145-2C11, RB6-8C5, M1/70, RA3-6B2, Ter-119;FC;https://www.biolegend.com/de-de/products/fitc-anti-mouse-lineage-cocktail-with-isotype-ctrl-5803
8;CD11b;BV421;BioLegend;101236;mouse, human, chimpanzee, baboon, cynomolgus, rhesus, rabbit;rat;monoclonal; M1/70;FC;https://www.biolegend.com/de-de/products/brilliant-violet-421-anti-mouse-human-cd11b-antibody-7163
9;CD11b;PE/Cy7;BD Pharmingen;552850;mouse, human, chimpanzee, baboon, cynomolgus, rhesus, rabbit;rat;monoclonal; M1/70;FC;https://www.bdbiosciences.com/eu/applications/research/stem-cell-research/mesenchymal-stem-cell-markers-bone-marrow/mouse/negative-markers/pe-cy7-rat-anti-cd11b-m170/p/552850
10;CD140a/PDGFRa;APC;R&D Systems;AF1062;mouse;mouse;polyclonal;NA;WB, IHC;https://www.rndsystems.com/products/mouse-pdgf-ralpha-antibody_af1062

11;CD140b/PDGFRb;APC;eBioscience;17-1402-82;mouse;rat;monoclonal;APB5;FC;https://www.thermofisher.com/antibody/product/CD140b-PDGFRB-Antibody-clone-APB5-Monoclonal/17-1402-80
12;CD171/L1CAM;PE-Vio770;Miltenyi;130-102-135;mouse;rat;monoclonal;555;FC, IF;https://www.miltenyibiotec.com/US-en/products/macs-flow-cytometry/antibodies/primary-antibodies/cd171-l1cam-antibodies-mouse-555-1-10.html/
13;CD24 ;PE/Cy7;Biolegend;101822;mouse;rat;monoclonal; M1/69;FC;https://www.biolegend.com/en-us/products/pe-cy7-anti-mouse-cd24-antibody-3862
14;CD2;APC;Biolegend;100112;mouse;rat;monoclonal;RM2-5;FC;https://www.biolegend.com/en-ie/products/apc-anti-mouse-cd2-antibody-9287
15;CD2;PE/Cy7;BioLegend;100114;mouse;rat;monoclonal;RM2-5;FC;https://www.biolegend.com/de-de/products/pe-cy7-anti-mouse-cd2-antibody-9288
16;CD31;Pacific Blue;Biolegend;102422;mouse;rat;monoclonal;390;FC;https://www.biolegend.com/de-de/products/pacific-blue-anti-mouse-cd31-antibody-6669
17;CD31;APC;BD Biosciences;551262;mouse;rat;monoclonal;MEC 13.3;FC;http://www.bdbiosciences.com/eu/applications/research/stem-cell-research/cancer-research/mouse/apc-rat-anti-mouse-cd31-mec-133/p/551262
18;CD31;APC;BioLegend;102510;mouse;rat;monoclonal;MEC 13.3;FC;https://www.biolegend.com/de-de/products/apc-anti-mouse-cd31-antibody-375
19;CD31;BV421;BD;562939;mouse;rat;monoclonal;MEC 13.3;FC;http://www.bdbiosciences.com/us/applications/research/stem-cell-research/cancer-research/mouse/bv421-rat-anti-mouse-cd31-mec-133/p/562939
20;CD31;FITC;BD Biosciences;561813;mouse;rat;monoclonal;MEC 13.3;FC;https://www.bdbiosciences.com/us/applications/research/stem-cell-research/cancer-research/mouse/fitc-rat-anti-mouse-cd31-mec-133/p/561813
21;CD31;FITC;Biolegend;102506;mouse;rat;monoclonal;MEC 13.3;FC;https://www.biolegend.com/de-de/products/fitc-anti-mouse-cd31-antibody-377
22;CD31;PE/Dazzle594;Biolegend;102526;mouse;rat;monoclonal;MEC 13.3;FC;https://www.biolegend.com/de-at/products/pe-dazzle-594-anti-mouse-cd31-antibody-14322
23;CD326;APC/Fire750;Biolegend;118230;mouse;rat;monoclonal;G8.8;FC;https://www.biolegend.com/en-us/products/apc-fire-750-anti-mouse-cd326-ep-cam-antibody-13635
24;CD326;PE/Cy7;Biolegend;118216;mouse;rat;monoclonal;G8.8;FC;https://www.biolegend.com/en-us/products/pe-cy7-anti-mouse-cd326-ep-cam-antibody-5303
25;CD34;AF647;BD Pharmingen;560230;mouse;rat;monoclonal;RAM34;FC;http://www.bdbiosciences.com/us/applications/research/stem-cell-research/cancer-research/mouse/alexa-fluor-647-rat-anti-mouse-cd34-ram34/p/560230
26;CD3;APC;Biolegend;100236;mouse;rat;monoclonal;17A2;FC;https://www.biolegend.com/en-us/products/apc-anti-mouse-cd3-antibody-8055
27;CD3;FITC;BioLegend;100203;mouse;rat;monoclonal;17A2;FC;https://www.biolegend.com/de-de/products/fitc-anti-mouse-cd3-antibody-45
28;CD44;APC;Biolegend;103012;mouse, human;rat;monoclonal;IM7;FC;https://www.biolegend.com/de-de/products/apc-anti-mouse-human-cd44-antibody-312
29;CD45;Pacific Blue;Biolegend;103126;mouse;rat;monoclonal;30-F11;FC;https://www.biolegend.com/de-de/products/pacific-blue-anti-mouse-cd45-antibody-3102
30;CD45;APC;Biolegend;103112;mouse;rat;monoclonal;30-F11;FC;https://www.biolegend.com/de-de/products/apc-anti-mouse-cd45-antibody-97
31;CD45;BV51;Biolegend;103138;mouse;rat;monoclonal;30-F11;FC;https://www.biolegend.com/de-de/products/brilliant-violet-510-anti-mouse-cd45-antibody-7995
32;CD45;FITC;BioLegend;103108;mouse;rat;monoclonal;30-F11;FC;https://www.biolegend.com/de-de/products/fitc-anti-mouse-cd45-antibody-99
33;CD45;PE;Biolegend;103106;mouse;rat;monoclonal;30-F11;FC;https://www.biolegend.com/de-de/products/pe-anti-mouse-cd45-antibody-100
34;CD45;PE/Cy7;eBioscience;25-0451-82;mouse;rat;monoclonal;30-F11;FC;https://www.thermofisher.com/antibody/product/CD45-Antibody-clone-30-F11-Monoclonal/25-0451-81
35;CD45R/B220;FITC;BioLegend;103206;mouse,human,cat;rat;monoclonal; RA3-6B2;FC;https://www.biolegend.com/en-us/products/fitc-anti-mouse-human-cd45r-b220-antibody-445
36;CD49f ;APC;Biolegend;313616;Human, African Green, Mouse, Baboon, Capuchin Monkey, Cat (Feline), Cattle (Bovine, Cow), Chimpanzee, Cynomolgus, Dog (Canine), Horse (Equine), Rabbit (Lapine), Rhesus, Sheep (Ovine), Swine (Pig, Porcine);rat;monoclonal;GoH3;FC;https://www.biolegend.com/de-de/products/apc-anti-human-mouse-cd49f-antibody-5617
37;CD66a;PE;Biolegend;134506;mouse;mouse;monoclonal;Mab-CC1;FC;https://www.biolegend.com/de-de/products/pe-anti-mouse-cd66a-ceacam1a-antibody-5986
38;CD90.2/Thy-1.2;APC/Cy7;Biolegend;105328;mouse;rat;monoclonal;30-H12;FC;https://www.biolegend.com/de-de/products/apc-cy7-anti-mouse-cd90-2-antibody-6671
39;CD90.2/Thy-1.1;AF488;BioLegend;202506;Rat, Mouse (AKR/J, PL, and FVBIN mouse strains), Cross-Reactivity: Rabbit (Lapine), Guinea Pig;mouse;monoclonal; OX-7 ;FC;https://www.biolegend.com/de-de/products/alexa-fluor-488-anti-rat-cd90-mouse-cd90-1-thy-1-1-antibody-3126
40;CD90.2/Thy-1.2;FITC;BioLegend;140304;mouse;rat;monoclonal; 53-2.1;FC;https://www.biolegend.com/de-de/products/fitc-anti-mouse-cd90-2-thy-1-2-antibody-6761
41;C-FMS ;BV411;Biolegend;135513;mouse;rat;monoclonal;AFS98;FC;https://www.biolegend.com/de-de/products/brilliant-violet-421-anti-mouse-cd115-csf-1r-antibody-8971
42;CKIT ;APC;BioLegend;105812;mouse;rat;monoclonal; 2B8;FC;https://www.biolegend.com/de-de/products/apc-anti-mouse-cd117-c-kit-antibody-72
43;endomucin;FITC;eBioscience ;14-5851-82;mouse;rat;monoclonal;V.7C7;FC, IHC, IP, WB;https://www.thermofisher.com/antibody/product/Endomucin-Antibody-clone-eBioV-7C7-V-7C7-Monoclonal/14-5851-81
44;EpCAM;APC;ThermoFisher;17-5791-82;mouse;rat;monoclonal;G8.8;FC, IHC, IP, WB;https://www.thermofisher.com/antibody/product/CD326-EpCAM-Antibody-clone-G8-8-Monoclonal/17-5791-80
45;EpCAM;FITC;eBioscience;11-5791-82;mouse;rat;monoclonal;G8.8;FC, IHC, IP, WB;https://www.thermofisher.com/antibody/product/CD326-EpCAM-Antibody-clone-G8-8-Monoclonal/11-5791-80
46;TER119;Pacific Blue;Biolegend;116232;mouse;rat;monoclonal;TEr-119;FC;https://www.biolegend.com/de-de/products/pacific-blue-anti-mouse-ter-119-erythroid-cells-antibody-6137
47;IgM;PE/Cy7;BioLegend;406514;mouse;rat;monoclonal; RMM-1;FC;https://www.biolegend.com/de-de/products/pe-cy7-anti-

mouse-igm-6935
48;CD49f;FITC;BioLegend;313606;Human, African Green, Mouse, Baboon, Capuchin Monkey, Cat (Feline), Cattle (Bovine, Cow), Chimpanzee, Cynomolgus, Dog (Canine), Horse (Equine), Rabbit (Lapine), Rhesus, Sheep (Ovine), Swine (Pig, Porcine);rat;monoclonal;GoH3;FC;https://www.biolegend.com/de-de/products/fitc-anti-human-mouse-cd49f-antibody-2606
49;LNGFR;Vio770;Miltenyi;103110079;mouse,monkey,goat,dog,pig,sheep;mouse;monoclonal;ME20.4-1.H4;FC, IF;https://www.miltenyibiotec.com/US-en/products/macs-flow-cytometry/antibodies/primary-antibodies/cd271-lngfr-antibodies-human-me20-4-1-h4-1-11.html/
50;Ly-6A/E;Pacific Blue;BioLegend;108120;mouse;rat;monoclonal;D7;FC;https://www.biolegend.com/de-de/products/pacific-blue-anti-mouse-ly-6a-e-sca-1-antibody-3140
51;Ly-6G/Ly-6C/GR1;FITC;BioLegend;108405;mouse;rat;monoclonal; RB6-8C5;FC;https://www.biolegend.com/de-de/products/fitc-anti-mouse-ly-6g-ly-6c-gr-1-antibody-458
52;Ly-6G/Ly-6C/GR1;PE/Cy7;BioLegend;108416;mouse;rat;monoclonal; RB6-8C5;FC;https://www.biolegend.com/de-de/products/pe-cy7-anti-mouse-ly-6g-ly-6c-gr-1-antibody-1931
53;CD326;PE/Cy7;Biolegend;118216;mouse;rat;monoclonal;G8.8;FC;https://www.biolegend.com/de-de/products/pe-cy7-anti-mouse-cd326-ep-cam-antibody-5303
54;CD44;APC;Biolegend;103012;mouse, human;rat;monoclonal;IM7;FC;https://www.biolegend.com/de-de/products/apc-anti-mouse-human-cd44-antibody-312
55;CD45;Pacific Blue;Biolegend;103126;mouse;rat;monoclonal;30-F11;FC;https://www.biolegend.com/de-de/products/pacific-blue-anti-mouse-cd45-antibody-3102
56;CD66a;PE;Biolegend;134506;mouse;mouse;monoclonal;Mab-CC1;FC;https://www.biolegend.com/de-de/products/pe-anti-mouse-cd66a-ceacam1a-antibody-5986
57;O4;PE;Miltenyi;130-095-887;humam,mouse,rat;mouse;monoclonal;O4;FC, IF;https://www.miltenyibiotec.com/US-en/products/macs-flow-cytometry/antibodies/primary-antibodies/anti-o4-antibodies-human-mouse-rat-o4-1-11.html
58;SCA1;APC;Biolegend;122512;mouse;rat;monoclonal;E13-161.7;FC;https://www.biolegend.com/en-us/products/apc-anti-mouse-ly-6a-e-sca-1-antibody-3897
59;SCA1;FITC;Biolegend;122506;mouse;rat;monoclonal;E13-161.7;FC;https://www.biolegend.com/en-us/products/fitc-anti-mouse-ly-6a-e-sca-1-antibody-3894
60;SCA1;Pacific Blue;Biolegend;108120;mouse;rat;monoclonal;E13-161.7;FC;https://www.biolegend.com/pacific-blue-anti-mouse-ly-6a-e-sca-1-antibody-3140.html
61;SCA1;PE/Cy7;BioLegend;122514;mouse;rat;monoclonal;E13-161.7;FC;https://www.biolegend.com/pe-cy7-anti-mouse-ly-6a-e-sca-1-antibody-3898.html
62;SDC4;APC;Miltenyi;130-109-831;mouse;rat;monoclonal;REA640;FC, IF;https://www.miltenyibiotec.com/US-en/products/macs-flow-cytometry/antibodies/primary-antibodies/anti-syndecan-4-antibodies-mouse-rea640-1-10.html/
63;TER119;FITC;BioLegend;116205;mouse;rat;monoclonal;TER-119;FC;https://www.biolegend.com/en-us/products/fitc-anti-mouse-ter-119-erythroid-cells-antibody-1865
64;TER119;PE/Cy5;BioLegend;116210;mouse;rat;monoclonal;TER-119;FC;https://www.biolegend.com/en-us/products/pe-cy5-anti-mouse-ter-119-erythroid-cells-antibody-1868
65;Thbs1;APC;Fisher;MA5-13398;Bovine, Dog, Horse, Human, Mouse, Sheep, Pig, Rat;mouse;monoclonal;A6.1;FC, IHC, IF, IP, WB;https://www.thermofisher.com/antibody/product/Thrombospondin-1-Antibody-clone-A6-1-Monoclonal/MA5-13398
66;Tmem119 ;AF488;Abcam;ab210405;mouse;rabbit;monoclonal;106-6;FC;http://www.abcam.com/tmem119-antibody-106-6-microglial-marker-ab210405.html
67;VCAM;PE/Cy7;Biolegend;105720;mouse;rat;monoclonal;MVCAM.A;FC;https://www.biolegend.com/en-us/products/pe-cy7-anti-mouse-cd106-antibody-6135

Validation

We relied on validation provided by the manufacturer of each antibody. All antibodies were used according to the manufacturers specifications and recommended dilutions. For more information please refer to the links provided for each antibody.

Animals and other organisms

Policy information about studies involving animals; ARRIVE guidelines recommended for reporting animal research

Laboratory animals	C57J/B6 mice, male and female, with ages 1m, 3m, 12m, 18m, 21m, 24m and 30m
Wild animals	The study did not involve wild anumals
Field-collected samples	The study did not involve field-collected samples
Ethics oversight	All animal care and procedures were carried out in accordance with institutional guidelines approved by the VA Palo Alto Committee on Animal Research.

Note that full information on the approval of the study protocol must also be provided in the manuscript.

Flow Cytometry

Plots

Confirm that:

☒ The axis labels state the marker and fluorochrome used (e.g. CD4-FITC).

☒ The axis scales are clearly visible. Include numbers along axes only for bottom left plot of group (a 'group' is an analysis of identical markers).

☒ All plots are contour plots with outliers or pseudocolor plots.

☒ A numerical value for number of cells or percentage (with statistics) is provided.

Methodology

Sample preparation	Please see the supplemental text for extensive details regarding each organ.
Instrument	Sony SH800S for all organs except limb muscle and diaphragm, which were sorted on a BD Aria III.
Software	BD FACS Diva and the default SH800S software were used to collect data.
Cell population abundance	Please see the supplemental text for extensive details regarding each organ.
Gating strategy	Please see the index data for each organ.

☒ Tick this box to confirm that a figure exemplifying the gating strategy is provided in the Supplementary Information.